Winter 12-2020

A Functional Three-Dimensional Microphysiological Model of Myeloma Bone Disease

Richard Visconti
richard.visconti@student.shu.edu

A Functional Three-Dimensional Microphysiological Model of Myeloma Bone Disease

Dissertation submitted by

Richard J. Visconti

Dissertation Committee:
Jessica Cottrell, PhD, Mentor
Kyle Kolaja, PhD
J. Patrick O'Connor, PhD
Allan Blake, PhD
Constantine Bitsaktsis, PhD

A dissertation submitted in partial fulfillment of the requirements for the degree of
Doctor of Philosophy, Molecular Bioscience
Department of Biological Sciences
Seton Hall University

December 2020

SETON HALL UNIVERSITY

College of Arts and Sciences

Department of Biological Sciences

APPROVAL FOR SUCCESSFUL DEFENSE

Richard Visconti has successfully defensed and finalized the text of his doctoral dissertation for the Ph.D during this Fall Semester 2020.

DISSERTATION COMMITTEE

(please sign and date beside your name)

_____

JESSICA COTTRELL, MENTOR

_____

CONSTANTINE BITSAKTSIS, COMMITTEE MEMBER

_____

ALLAN BLAKE, COMMITTEE MEMBER

_____

KYLE KOLAJA, COMMITTEE MEMBER

_____

J.PATRICK O'CONNOR, COMMITTEE MEMBER

_____

DANIEL BRIAN NICHOLS, DIRECTOR OF GRADUATE STUDIES

_____

HEPING ZHOU, CHAIRPERSON, DEPARTMENT OF BIOLOGICAL SCIENCES

The mentor and any other committee members who wish to review revisions will sign and date this document only when revisions have been completed.

Acknowledgements

With a great deal of admiration and respect, I humbly thank everyone that helped me during this scientific journey. Especially those that provided motivation, guidance, and support: Dr. Jessica Cottrell, Dr. Kyle Kolaja, Dr. Allan Blake, Dr. Constantine Bitsaktsis, and Dr. J. Patrick O'Connor.

Dr. Cosimo Antonacci, SHU Chemistry Department, was extremely helpful in performing the FTIR analysis and Deboleena Kanjilal, Rutgers University Medical School, kindly performed the micro-CT analysis.

I'd also like to acknowledge the esteemed faculty and administrators of Seton Hall University, especially those in the department of Biological Sciences for providing knowledge and enlightenment.

I salute all of my colleagues and wish them success and happiness through their respective graduate programs and beyond.

Lastly, I'd like to thank my family, especially my wife Jennifer, for the never-ending patience, support, and love.

Table of Contents

Abbreviations

3D	Three-Dimensional
3D-NBF	Three-Dimensional Normal Bone-Like Fragment
3D-MBD	Three-Dimensional Myeloma Bone Disease
AP	Alkaline Phosphatase
AR	Alizarin Red
BMM	Bone Marrow Macrophages
BMP	Bone Morphogenic Protein
BMSC	Bone Marrow Stromal Cell
BMU	Basic Multicellular Unit
CTX-1	C-Terminal Telopeptides Type Collagen 1
DKK1	Dickkopf-related Protein 1
ECM	Extracellular Matrix
HA	Hydroxyapatite
HDAC	Histone Deacetylase
IMiD	Immunomodulatory Drug
LGR	Leucine-Rich Repeat-Containing G-Protein Coupled Receptor
MAPK	Mitogen-Activated Protein Kinases
M-CSF	Macrophage Colony Stimulating Factor
MCP-1	Monocyte Chemoattractant Protein-1
MIP-1	Macrophage Inflammatory Protein-1
MM	Multiple Myeloma
MBD	Myeloma Bone Disease
MSC	Mesenchymal Stem Cell
OB	Osteoblast
OC	Osteoclast
OL	Osteolytic Lesion
OPG	Osteoprotegerin
PI3K	Phosphatidylinositol 3-Kinase

PHO	Primary Human Osteoblast
PTH	Parathyroid Hormone
RANKL	Receptor Activator of Nuclear factor Kappa-B Ligand
TAK1	TGF-β Activated Kinase 1
TGF-β	Transforming Growth Factor-β
TRAF	TNF receptor-associated factor
TRAcP5b	Tartrate-Resistant Acid Phosphatase 5b
WNT	Wingless and Int-1 signaling pathway

Abstract

Multiple myeloma (MM) is a hematologic cancer caused by a mature B cell neoplasm, or plasmacytoma, that infiltrates the skeleton at several sites. The disease is characterized by uninhibited transformed plasma cell proliferation that disrupts skeletal homeostasis leading to decreased bone modeling and increased bone resorption. Osteolytic lesions (OL) or voids left in the bone, remain long after the treatment of the cancer and indicate disease progression to myeloma bone disease (MBD). Current combinatorial MM therapies inhibit malignant plasma cell proliferation, slow the progression towards MBD, and increase the mean five-year survival rate, but do little to improve osteoblastic function and restore skeletal homeostasis. Conversely, several novel MBD treatments have been developed to heal OLs, including monoclonal antibodies that target receptor activator of nuclear factor kappa-B ligand (RANKL) and sclerostin.

A functional in vitro three-dimensional (3D) microphysiological human MM bone model was developed to aid in the identification of improved combinatorial treatments that suppress plasma cell proliferation while healing osteolytic lesions. Bone Marrow Stromal Cell-derived (BMSC) osteoblasts and Bone Marrow macrophage-derived osteoclasts maintained as a homeostatic coculture capable of bone formation and resorption form mineralized bone fragments. The introduction of human plasmacytoma cell lines induce lesions in the Mini-bones decreasing the cumulative hydroxyapatite (HA) content while increasing resorption markers, like C-Terminal Telopeptides Type Collagen 1 (CTX-1) recapitulating physiological conditions of MBD. 3D myeloma disease-induced bone fragments treated with a combination of immunomodulatory and bone modifying agents had lower free CTX-1 and more HA present after twelve days of

exposure. These alterations in bone integrity and resorption were dose-dependent and demonstrated the model's potential to evaluate novel combinatorial therapies.

List of Figures

Introduction

1.1 Bone Formation and Remodeling

Osteogenesis or bone formation is a process that is controlled by local and systemic regulatory factors. It occurs in three distinct phases: synthesis of an extracellular organic matrix (osteoid), matrix mineralization, and remodeling comprised of resorption and reformation. There are three cell types ultimately responsible for bone modeling and resorption. Osteoblasts are responsible for bone matrix synthesis and mineralization [1]. They are derived from mesenchymal stem cells and are subject to local canonical Wnt signaling for migration, differentiation, proliferation, and survival. Some osteoblasts encased by the matrix, in a chamber called a lacunae, differentiate into osteocytes. Osteocytes support bone structure and metabolism by continued matrix production and mechanosensation. The latter is supported by a system of canaliculi that connect a series of osteocytes and the Wnt signaling pathway. Osteoclasts, polykaryonic cells derived from monocytic fusion, migrate from the marrow to the bone surface where they are responsible for bone degradation during the resorptive phase of bone remodeling.

Human cortical and trabecular/cancellous bone is formed through two different processes called endochondral and intramembranous ossification. Although endochondral ossification occurs through a cartilage precursor and each process forms different bone of the skeleton, both require osteoblastic deposition of osteoid, the organic component of bone matrix that is 90-95% collagenous protein or ossein, noncollagenous proteins, and growth factors. Ossified bone is comprised of roughly twenty to thirty percent osteoid, sixty to seventy percent hydroxyapatite, and ten percent water. Hydroxyapatite ($Ca10(PO4)_6(OH)_2$), a natural form of calcium phosphate, mineralizes the osteoid and gives the bone rigidity.

Human bones are maintained through a biological process, known as remodeling, that occurs in five stages activation, resorption, formation, mineralization, and quiescence. The activation phase of the bone remodeling process is initiated through direct mechanical stress/loss of structural integrity, osteocyte apoptosis, or through hormonal signaling via estrogen and parathyroid hormone (PTH) secretion. PTH binds its cognate receptor of bone lining preosteoblastic cells located in the cambium layer of the periosteum at the remodeling site. This molecular signaling cascade activates protein kinases A and C and causes GPCR-mediated calcium release from the endoplasmic reticulum [2]. Downstream transcriptional factors ultimately lead to the secretion of osteoclast recruitment molecules like monocyte chemoattractant protein-1 (MCP-1) and cell-surface antigen A7 [3]. One of the ways osteocytes regulate the remodeling process is through the secretion of TGF-β, an osteoclastogenesis inhibitor. The loss of viable osteocytes decreases local levels of TGF-β, promoting osteoclast differentiation and recruitment. Cells of the periosteum work in conjunction with other osteogenic cells to form basic multicellular units (BMUs) that form a cellular canopy over the remodeling compartment [2].

Macrophage Colony Stimulating Factor (M-CSF) binds the c-FMS receptor on Bone Marrow Macrophages (BMM) and initiates phosphorylation of tyrosine residues located in c-FMS's cytoplasmic tail leading to activation of phosphatidylinositol 3-kinase (PI3K) and Akt. These signaling cascades lead to enhanced proliferation and survival signaling, induce cellular fusion, and upregulates receptor activator of nuclear factor kappa B (RANK) expression [4]. When RANK ligand (RANKL) binds RANK, this receptor elicits TNF receptor-associated factor (TRAF) recruitment. The TRAF6-RANK signaling complex combines with TGF-β activated kinase 1 (TAK1) and TAK-1 binding protein (TAB2) that activate downstream mitogen-

activated protein kinase (MAPK) signaling pathways including: nuclear factor kappa B (NF-κB), c-Jun N-terminal kinase (JNK), and extracellular signal-regulated kinase (ERK) that lead to upregulation genes that control osteoclast differentiation [4].

Once osteoclasts localize to the remodeling compartment, they become part of the BMU and the resorptive phase begins. Osteoclasts adhere to the bone surface through an actin-rich structure called a podosome. Upon attachment osteoclasts polarize, form a tight seal, and acidify the bone surface through the secretion of hydrogen ions. The acidic environment demineralizes and exposes the bones extracellular matrix (ECM) [5].

Osteoclasts also secrete a protease that catabolizes collagen, elastin, and gelatin called cathepsin K. This protease denudes the remaining matrix and forms the resorption lacunae [6]. This proteolytic decomposition also liberates osteogenic signaling molecules, like transforming growth factor β (TGF-β) embedded in the matrix by osteoblasts during bone formation. The entire resorption phase of bone remodeling takes approximately 3 weeks in humans [7].

The reversal phase of bone remodeling, which takes approximately 1-2 weeks, is a transitional period. Resorption activity is halted while the bone microenvironment conditions become favorable for osteoblast differentiation, migration, and bone formation. Three primary events mark the reversal phase of bone remodeling: osteoclasts undergo apoptosis, peripheral macrophages clear the resorption zone and prime it for bone formation, and osteoblasts differentiate and localize to the denuded bone's resorption site, Howship's lacunae [5].

The formation phase of bone remodeling is initiated through several signaling mechanisms. Canonical Wnt signaling plays an integral part from osteoblastogenesis, to proliferation and matrix formation, through the mineralization process. R-spondin 2 (Rspo2) is a Wnt receptor agonist and

positive autocrine regulator of osteoblastogenesis. Rspo2 binding to a Leucine-Rich Repeat-Containing G-Protein Coupled Receptor (LGR) expressed on the cell membrane causes an interaction with the coreceptor, Frizzled, which causes components of the destruction complex to relocate to the plasma membrane. The destruction complex consists of glycogen synthase kinase 3 (GSK-3), casein kinase 1 (CK1), the scaffolding protein Axin, the adenomatous polyposis coli (APC) protein, and the E3-ubiquitin ligase β-TrCP, which together phosphorylates β-catenin and elicits proteasomal degradation of the protein [8]. The LGR-Frizzled interaction dissociates APC from the destruction complex and inhibits GSK-3 phosphorylation of β-catenin. The free β-catenin accumulates in the cytoplasm and translocates to the nucleus where it promotes expression of osteogenic genes that induce Bone Marrow Stromal Cells (BMSC), or mesenchymal stem cells, to differentiate into preosteoblasts. Continued canonical Wnt signaling stimulation completes the differentiation process and promotes functionality in osteoblasts [9].

TGF-β family members like TGF-β and Bone Morphogenic Protein (BMP) play an integral role in bone formation through canonical Smad-dependent and independent signaling pathways. Osteoclasts liberate latent TGF-β stored in the ECM during the resorptive phase of bone remodeling. The latent TGF-β becomes activated due to acidic pH of the bone remodeling compartment [10]. Active TGF-β binds type I and II TGF-β receptors (TβRI and TβRII) on the surface of BMSCs initiating osteoblastogenesis. Once bound TβRII is bound by ligand it transphosphorylates TβRI and initiates S signaling. Smad dependent signaling occurs when the phosphorylated R-Smads (rSmad2 or rSmad3) form a complex with Smad4. This complex then translocates to the nucleus and interacts with transcription factors like RUNX2 to upregulate the expression of osteogenic target genes [11]. TGF-β also activates the non-Smad dependent TAK1 signaling pathway during bone formation when ligand-bound PTH receptor forms a complex with

TβRII, facilitates internalization, and activates TAK1 [12]. TAK1 causes downstream phosphorylation and activation of the p38 mitogen-activated protein kinases (MAPK) pathways that converge at RUNX2 regulating expression of essential osteogenic genes [13]. Other anabolic factors, such as lactoferrin, enhance TGF-β receptor expression and contribute to BMSC osteoblastogenesis [14].

The Wnt/β-catenin, TGF-β, and BMP signaling work in concert to promote BMSC differentiation into pre-osteoblasts and maturation into functional osteoblasts. These mature osteoblasts localize to the denuded bone and secrete osteoid, the unmineralized organic portion of bone primarily composed of type I collagen, chondroitin sulfate, and osteocalcin [15]. The bone formation process takes several months to complete [16].

As osteoblasts migrate to the remodeling site on the denuded bone they attach, secrete bone matrix proteins like type 1 collagen, osteopontin, and osteocalcin. Osteoblasts also localize alkaline phosphatase (AP) on the apical side of their membrane to regulate phosphate production essential for mineralization [17]. As osteoblasts advance along the cement line, the site at which new bone is formed and osteoblasts and osteocytes interact through canaliculi, they group and form an osteon. New bone is formed through cellular and molecular mechanisms within osteoblasts that include: alkaline phosphatase hydrolysis of pyrophosphate to inorganic phosphate essential for HA crystal formation and the accumulation of calcium within matrix vesicles (Figure 1). When the accumulation of calcium and phosphate exceed the solubility point HA crystals form and extend into the extracellular space where the mineral is deposited in the collagen-rich ECM leading to ossification or formation of new bone [18]. The mineral formation equation is as follows:

$6HPO_4^{2-} + 2H_2O + 10\ Ca^{2+} \rightarrow Ca_{10}(PO_4)_6(OH)_2 + 8H^+$

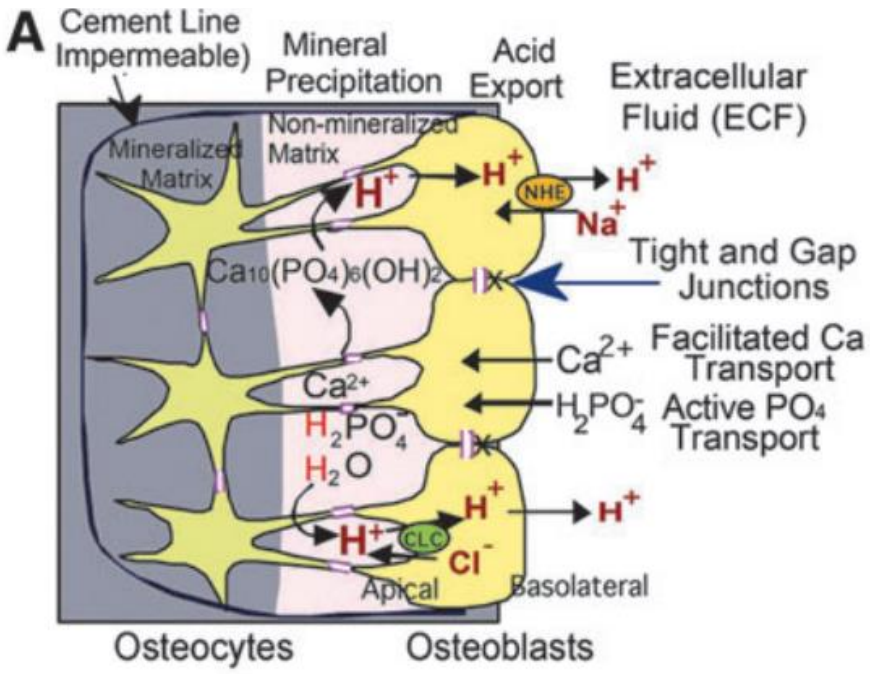

Figure 1. Major Mechanism of Osteoblastic Transport and Mineralization. Hydroxyapatite, a critical component in bone mineralization, is formed by polarized osteoblasts when bone alkaline phosphatase, found on the outer surface of membrane vesicles, hydrolyzes calcium and inorganic phosphate. The HA crystals form, grow, and eventually penetrate the membrane vesicles exposing them to the collagen-rich extracellular bone matrix where they are deposited. The process requires active and passive transport exemplified through acid uptake by CIC exchangers at the apical membrane and basolateral acid transcytosis through NHE exchangers [17].

1.2 Myeloma Bone Disease

Multiple myeloma (MM), one of the most prevalent hematologic cancers in the United States [19], is a plasma cell cancer characterized by malignant bone infiltration, hypercalcemia, anemia, increased susceptibility to infection, and kidney failure. Early stage MM is primarily asymptomatic and is typically identified serendipitously through laboratory diagnostic blood or imaging tests. Osteolytic lesions (OLs), regions of decreased bone density or "softening," are detected in over 80% of MM patients upon initial diagnosis [20]. These regions of poor bone

density arise from an imbalance in normal bone homeostasis which is brought on by MM and can lead to myeloma bone disease (MBD).

MBD causes fatigue and constant bone pain that cannot be relieved with anti-inflammatory agents or rest [21]. This persistent pain is often the impetus for the initial visit to a primary care physician that eventually leads to the official MM/MBD diagnosis. The spine is the predominant site of OLs and pain is often induced through direct contact between the tumor and the nerves. MBD-associated lesions also weaken bones, cause spinal cord compression, and increase incidents of pathologic fractures [22]. Although the precise mechanism of plasmacytoma-mediated bone remodeling disruption is not fully understood, normal skeletal homeostasis has been studied for decades.

The mechanism by which MBD OLs are derived include the release of the aforementioned osteoclast stimulatory factors and osteoblast inhibitory factors (Figure 2). The primary mechanism of osteoclast stimulation is through secretion of receptor activator of nuclear factor kappa-B ligand (RANKL) [23]. MM cells directly induce osteoclast activation and inhibit osteoblasts through secretion of several cytokines including: decoy receptor 3 (DcR3), interleukin-3 (IL-3), macrophage inflammatory protein-1 alpha (MIP-1α), macrophage inflammatory protein-1 beta (MIP-1β), and tumor necrosis factor-alpha (TNF-α). MIP-1α is a chemokine produced by MM cells in approximately 70% of patients and correlates with an extremely poor prognosis [24]. MIP-1α is known to potentiate both osteoclast formation and RANKL secretion [25]. TNF-α is a cytokine capable of eliciting osteoclast formation while suppressing osteoblast differentiation. IL-3 is known to augment osteoclastogenesis by enhancing RANKL and MIP-1α function [23]. IL-3 is also elevated in the majority of MM patient's bone marrow plasma samples. MM cells also inhibit osteoblast function through

secretion of factors like the Wnt inhibitor, Dickkopf-related protein 1 (DKK1), and secreted frizzled-related protein 2 (sFRP2) [26]. DKK1 blocks osteoblast proliferation and differentiation by sequestering the canonical Wnt signaling ligand in preosteoblasts [25]. Overall, MM OLs are known to release factors that promote osteolytic resorption of bone while preventing new osteoblast deposition.

Plasmacytoma cells also inhibit osteoblastogenesis and new bone formation through aberrant expression of Wnt receptors that sequester Wnt agonists essential for osteogenic signaling [27]. MM cells also secrete sclerostin, a cysteine knot-containing protein, that activates caspase signaling and induces apoptosis in mature osteoblasts [28].

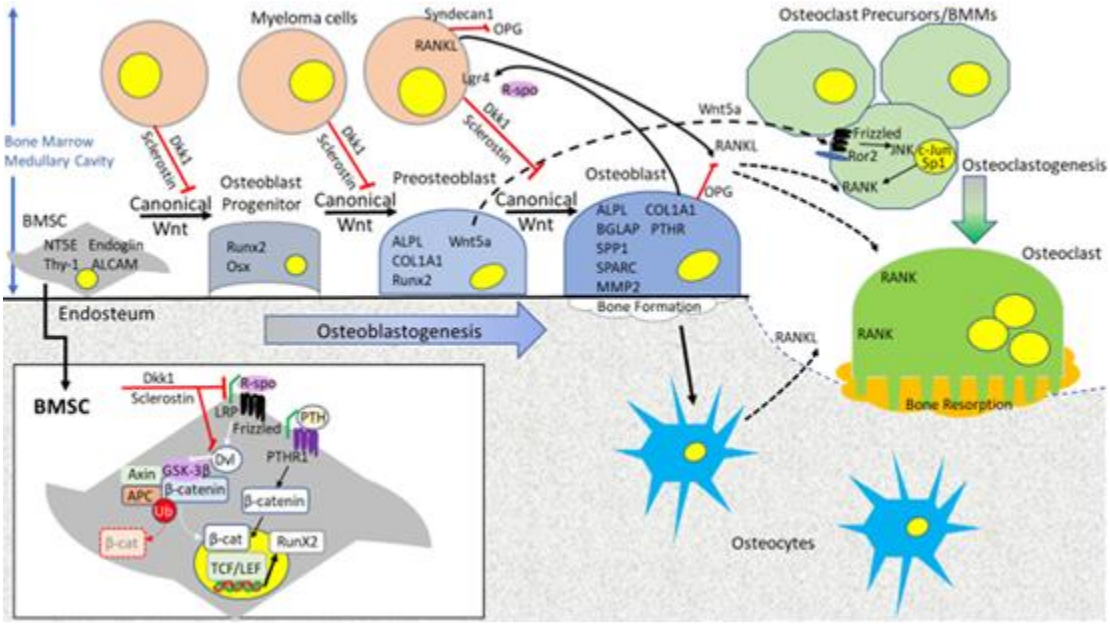

Figure 2. Molecular Signaling of Multiple Myeloma. MM cells disrupt bone remodeling homeostasis through direct and indirect mechanisms that promote enhanced osteoclastic differentiation and bone resorption while inhibiting osteoblastogenesis and bone formation. This occurs through secretion of a number of signaling factors, like cytokines and RANK ligand, and soluble proteins, like the Wnt inhibitor DDK-1 and the RANKL decoy receptor, osteoprotegerin (OPG) [29].

1.3 MM/MBD Therapeutic Intervention

According to the American Cancer Society, there are six different classes of drugs that are commonly used to treat MM: chemotherapeutics, corticosteroids, immunomodulating agents, proteasome inhibitors, histone deacetylase inhibitors, and monoclonal antibodies. Chemotherapeutic agents nonspecifically destroy proliferating cells through several different molecular mechanisms. Melphalan and cyclophosphamide are alkylating agents that chemically inhibit nucleic acid synthesis [30]. While Vincristine binds the mitotic spindle and inhibits microtubule formation [31]. Doxorubicin inhibits topoisomerase II progression, an enzyme that uncoils DNA during replication, halting cell division [32]. All these drugs elicit systemic cytotoxicity in MM patients but have adverse side effects like nausea, vomiting, and low blood cell counts and can cause permanent damage to organs.

Corticosteroids, like dexamethasone and prednisone, are synthetic steroids used to mitigate the effect of immune response on nontarget tissues by decreasing inflammation and swelling [33]. Corticosteroids alleviate some side effects caused by chemotherapeutics and have been reported to improve the effectiveness of some treatments. Immunomodulating agents are thalidomide analogs, like lenalidomide and pomalidomide, that cause ligand-dependent degradation of B cell transcription factors necessary for cell survival and proliferation [34]. They are quite effective at inhibiting plasma cell division, but they do not cure the disease. Proteasome inhibitors, like bortezomib and carfilzomib, block enzymatic degradation of eukaryotic proteins essential for cell growth and division [35]. Cancer cells have been reported to have higher proteasome activity. Serious side effects, like nausea, vomiting, low blood cell counts, and neuropathy have been associated with several proteasome inhibitors. Although this class of drugs was initially utilized in patients with refractory disease, they are now commonly

included in combinatorial treatment strategies. Histone deacetylase (HDAC) inhibitors, like panibostat and vorinostat, affect gene regulation through interactions with chromosomal histones that wrap around chromatin and regulate the efficiency of transcription [36]. HDAC inhibitors were initially used to treat patients that relapsed after treatments with immunomodulating agents and proteasome inhibitors but are now incorporated into some combinatorial treatment regimes. The last class of drugs currently used to treat MM contains various monoclonal antibodies, like daratumumab and elotuzumab. These antibodies target surface markers on neoplastic plasma cells and elicit a host immune response to the cancer [37]. Several new antibody-based treatments currently in the clinic focus on bispecific T cell engagement, antibody-drug conjugates, checkpoint inhibition, and chimeric antigen receptor T cell therapy.

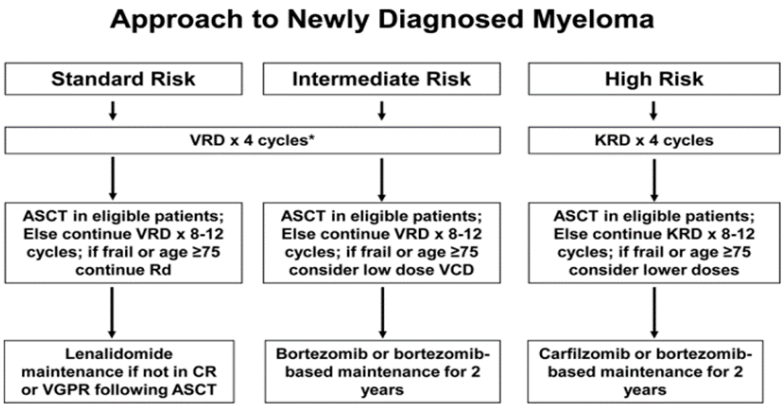

Figure 3. MM Standard of Care. The strategy behind the MM standard of care is a combinatorial drug regimen that includes IMiDs, proteasome inhibitors, corticosteroids, and chemotherapeutic agents [38]. Velcade (bortezomib), Revlimid (lenalidomide), and Dexamethasone are used in standard and intermediate risk patients. Kyprolis (carfilzomib) is often the proteasome inhibitor of choice for high risk patients. Autologous Stem Cell Transplants (ASCT) is widely used in eligible patients regardless of MM risk stratification.

A paper published in Mayo Clinic Proceedings 2016 by Rajkumar and Kumar detailed the most common therapies for treating newly diagnosed MM (Figure 3). Common MBD treatments include combinations of the MM drugs and bone strengthening agents. These agents

promote osteoblastogenesis and differentiation, decrease osteoclastogenesis, and induce apoptosis in osteoclasts. Most drugs were developed primarily to treat osteoporosis but are currently being tested as novel therapies in MBD. Bisphosphonates, like pamidronate and zoledronate, elicit Fas-mediated apoptosis through caspase 3/7 activation in mature osteoclasts [39]. This osteoclastic cell death reduces bone resorption, but bisphosphonate MBD treatment has been associated with adverse side effects such as osteonecrosis of the jaw [40]. Activin A inhibitors, like sotatercept, function by blocking the transcription of receptor activator of nuclear factor kappa-B (RANK) which is essential in osteoclast differentiation. Elevated levels of Activin A have been found in myeloma patients [24] and use of Activin A inhibitors have been shown to induce bone formation and inhibit cancer-related bone damage *in vivo* [41]. Teriparatide, a bioactive hormonal analog of para thyroid hormone (PTH), selectively activates osteoblasts. PTH is the primary source of calcium and phosphate metabolism in the bone and kidney [42]. Teriparatide, a biosynthetic form of PTH, also inhibits sclerostin (SOST), a WNT inhibitor that targets LRP4/LRP5-6 and antagonizes canonical Wnt signaling by binding to the LRP5/6 receptor. Teriparatide promotes osteoblast proliferation survival through PTH receptor signaling mentioned previously. Antibodies, like denosumab and romosozumab, have been used successfully to treat osteoporosis and have great potential in treating MBD. Denosumab blocks the RANK receptor on osteoclasts halting differentiation and subsequent bone resorption [43]. Romosozumab is an anti-sclerostin antibody that has a similar effect as teriparatide while avoiding the potential serious side effects, including vertigo and tachycardia.

Several new biotherapies have been developed to target pro-osteoclastic signaling molecules like RANKL, Denosumab. Some physicians also incorporate osteoporosis-targeting agents, including bisphosphonates to treat MBD. Bisphosphonates, like alendronate, inhibit farnesyl

pyrophosphate (FPP) synthase, disrupting the mevalonate pathway inhibiting the synthesis of isoprenoid intermediates culminating in osteoclast apoptosis [44].

1.4 The 3D Microphysiological Model of 3D Myeloma Bone Disease

Several recent publications utilize MM patient-derived BM aspirates to culture BMSCs in a 3D manner [45, 46] for use in personalized medicine to test combinatorial treatment regimens. This proposed 3D model of human myeloma bone disease focuses on disruption of normal bone remodeling through induction of the myeloma disease state through the addition of plasmacytoma cell lines. The normal homeostatic remodeling of the bone sets a quantifiable baseline of bone integrity. Formation and subsequent treatment of osteolytic lesions are measurable parameters to assess the effectiveness of MBD treatments at restoring normal bone remodeling and skeletal repair.

The 3D model of human myeloma bone disease described in this dissertation relies upon a co-culture of functional human osteoblasts and osteoclasts that engage in homeostatic bone formation and remodeling. Osteogenic differentiation of human BMSCs elicits formation of mineralized layers containing calcium deposits [47]. Three-dimensional in vitro models of osteogenically differentiated BMSCs show increased alkaline phosphatase activity and mineralization [48]. Others have used collagen-rich Matrigel to develop a 3D model of bone in different scaffolds [49] and co-cultured osteoblasts and osteoclasts in 3D to simulate the bone microenvironment [50].

This in vitro of model of normal homeostatic human bone remodeling was developed through prolonged culture of human BMSCs embedded in Matrigel, osteogenic differentiation into functional alkaline phosphatase-producing human osteoblasts, and subsequent

mineralization of ECM into a micro bone organoid (Figure 4). Osteogenic differentiation and osteoblast functionality will be assessed through alkaline phosphatase staining, alizarin red staining, and microscopic analysis. Mineralization and bone ossification will be quantified through an assay to measure HA content [51] and through confocal microscopy and micro-CT.

Since osteoclasts have a shorter lifespan than osteoblasts, 2 to 3 weeks compared to approximately 3 months [52], BMMs are added to the culture after approximately three weeks of osteogenic differentiation. BMM to osteoclast differentiation will be facilitated through the incorporation of RANKL and GM-CSF into the growth medium and cells will be grown for one month. Osteoclast functionality will be measured through an ELISA assay designed to detect a biomarker of bone resorption, CTX-1 [53]. Osteoclasts will also be characterized for the presence of osteogenic transcripts by RT-PCR/Taqman [54] and microscopic analysis of cell fusion resulting in multinucleation [55].

Once osteoblast and osteoclast functionality are confirmed, osteolytic lesions will be induced through the addition of human MM-derived plasmacytoma cell lines to the culture [56]. Plasmacytomas intensify resorption through the secretion on osteoclastic activating factors like RANKL and osteopontin and suppresses bone formation through sequestration of Wnt agonist and secretion of DKK1 [27]. Prolonged osteoclastic function yields increased levels of TRAcP 5b, liberates CTX-1 from the bone ECM, and decreases the amount of HA in the mineralized bone. OLs will also be monitored through confocal microscopic analysis.

Therapeutic intervention with commercially available MBD-targeting pharmaceutical agents will be used to treat the lesions with each respective drug and combinations of those included in the panel: lenalidomide, bortezomib, denosumab, and romosozumab. HA content, the

aforementioned biomarkers of bone resorption, and microscopic analysis of the lesions will be measured before and after treatment.

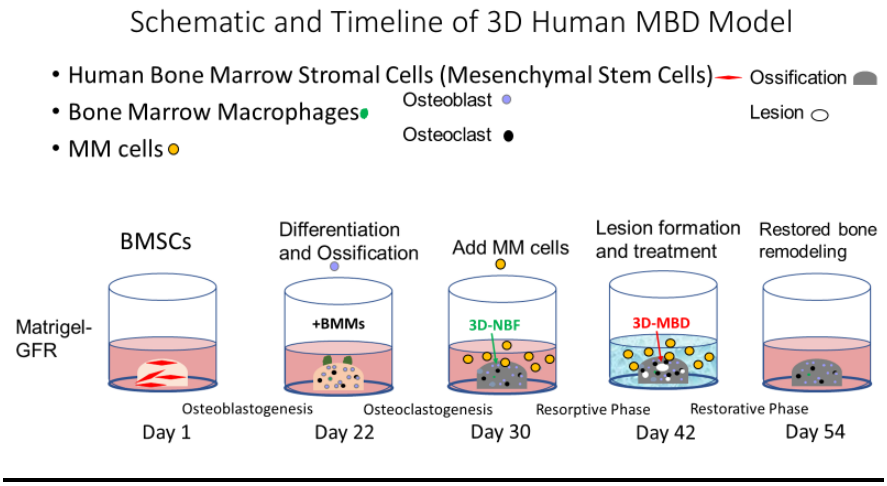

Figure 4. 3D *In Vitro* Model of Myeloma Bone Disease. Matrigel embedded BMSCs and BMMs differentiate into osteoblasts and osteoclasts respectively and maintain skeletal homeostasis through balanced bone formation and resorption forming 3D normal bone fragments (3D-NBF). Human MM-derived plasmacytoma cells disrupt the bone remodeling process by enhancing osteoclast and inhibiting osteoblast function eliciting a disease state in the bone fragments (3D-MBD).

Methods

2.1 3D in vitro Model of Normal Bone-Like Fragments (3D-NBF)

2.11 Primary human Bone Marrow Stromal/Mesenchymal Stem Cells (RoosterBio, cat# MSC 030) were rapidly thawed at 37°C, washed with OsteoMax-XF™ (Millipore Sigma, cat# SCM121), and seeded at 25,000 cells per 20 µl cold Matrigel™ GFR (Corning, cat# 356231). The cell suspension was kept on ice until it was pipetted as 20 µl droplets/domes into respective wells of a 96-well plate (Corning, 353219). The plate was incubated at 37°C for seven minutes to polymerize the gel and then 100 µl of OsteoMax-XF™ (Millipore Sigma, cat# SCM121) was carefully added to each well as not to disturb the integrity of the Matrigel droplet. Plates were returned to the incubator and cultured at 37°C in the presence of 5% CO_2 for twenty-one days, replacing 50% of the media with fresh OsteoMax-XF™ every two to three days.

2.12 On Day 21 primary human osteoclast precursors (Lonza, cat# 2T-110), bone marrow macrophages, were rapidly thawed at 37°C, washed with OsteoMax-XF™ and resuspended in OsteoMax-XF™ supplemented with RANKL 120 ng/ml (Sigma-Aldrich, cat# GF091) and GM-CSF 66 ng/ml (Sigma-Aldrich, cat# SRP6165-10UG), and seeded at 25,000 cells per well in 100 µl medium. Plates were returned to the incubator and cultured at 37°C in the presence of 5% CO_2 for an additional ten days, replacing 50% of the media with fresh OsteoMax-XF™ supplemented with RANKL and GM-CSF every two to three days.

2.13 Control cultures including: BMSCs grown in stem cell medium only (BMSC-), cell-free Matrigel cultured in the osteogenic differentiation medium (M+), HEK-293T cells in OsteoMax-XFTM (HEK293+), and Caco-2 cells grown in OsteoMax-XFTM (Caco2+) were cultured under the same conditions for over 30 days. The control samples were characterized simultaneously with the 3D-NBF samples.

2.2 3D in vitro Model of Human Myeloma-Diseased Bone

A human myeloma bone disease model was created by co-culturing the normal 3D-NBF samples with four different human lymphoblast, plasmacytoma, or myeloma cell lines for fourteen days. MM.1S (ATCC, CRL-2974), NCI-H929 (ATCC, CRL-9068), U266B1 (ATCC, TIB-196), RPMI 8226 (ATCC, CCL-155) were initially seeded at 0, 7,500, 10,000, 15,000 and 25,000 and at 50,000 cells per well in subsequent experiments. The mineralized 3D-NBF samples were cultured in the presence of the cancer cell lines for at least twelve days to promote enhanced bone resorption and the formation of osteolytic lesions. Subsequent experiments were conducted with RPMI 8226 cells seeded at 20,000 cells per well and remained in culture for at least twelve days.

2.3 Characterization of 3D in vitro Bone Models

2.31 Imaging/Microscopic Analysis of Mineralization

Osteoblast differentiation and bone mineralization were monitored kinetically through microscopic analysis on an Incucyte™ S3 (Essen Bioscience, cat#4647) with a 4x objective. Images were analyzed with Incucyte™ S3 software. Images were captured three times each day throughout the course of the entire osteogenic differentiation and mineralization process (30 days).

2.33 Phalloidin Staining

Samples were fixed in 4% formaldehyde (Pierce™ 16% Formaldehyde (w/v), Methanol-free Thermo Fisher Scientific, cat# 28906), stock was diluted in 1X DPBS, by removing media and washing each well with 1X Dulbecco's Phosphate Buffered Saline (DPBS). DPBS was aspirated and 100 µl of 4% formaldehyde was added to each well. Plates were fixed at room

temperature for 30 minutes. The 4% formaldehyde was aspirated and wells were washed three times with 1X DPBS. 200 µl per well of 1X Alexa Fluor™ 488 Phalloidin (Thermo Fisher Scientific, cat# A12379) and diamidino-2-phenylindole DAPI) (Thermo Fisher Scientific, cat#62248) was added to each well and plates were incubated at room temperature for 30 minutes. The staining solution was removed and wells were washed three times with 1X DPBS. Samples were stored in 300 µl 1x DPBS. Images were captured on a fluorescent microscope (Nikon Eclipse Ti).

2.34 Alkaline phosphatase (AP) staining

A wash buffer consisting of 0.05% Tween 20 (Sigma-Aldrich, cat# P9416) in 1X DPBS (with calcium and magnesium) (Thermo Fisher Scientific, cat#14040117) was made and used throughout the staining process. The AP substrate solution was prepared by dissolving a BCIP®/NBT tablet (Sigma-Aldrich, cat#B5655) in 10 ml distilled water (the solution was stored in the dark and used within two hours of preparation). Alkaline phosphatase staining was performed on 4% formaldehyde briefly-fixed, less than two minutes, bone and cell samples to retain AP activity post fixation. Samples were gently, yet thoroughly, washed twice immediately after fixation. Solutions were carefully aspirated as not to disturb the cell/bone samples. The AP substrate solution was added at 100 µl per well and plates were covered and incubated in the dark for ten minutes at room temperature. After incubation the plates were washed three times as previously described and samples were stored in 1X DPBS. Plates were immediately analyzed through light microscopy (Nikon Eclipse Ti) and images were captured.

2.35 Alizarin Red Staining

The spent medium was removed from each well and plates were washed twice with 200 ul 1X PBS. Samples were fixed in 4% formaldehyde for 30 minutes at room temperature. Fixative was removed and wells were washed three times with deionized water. Alizarin Red staining reagent (Millipore Sigma, cat#TMS-008-C) was added at 1X 40 mM concentration at 100 µl/well and plate was shaken gently for thirty minutes at room temperature. Alizarin red staining reagent was removed and plates were washed three times with deionized water. Plates were immediately analyzed through light microscopy (Nikon Eclipse Ti) and images were captured.

2.36 RT-PCR/Taqman™ Human Osteogenic and WNT signaling Pathway Array Plates

RNA samples were extracted from undifferentiated RoosterBio BMSCs, primary human osteoblasts isolated from femoral trabecular bone tissue from the knee or hip joint region PromoCell, cat# C12720), and the 3D-NBF and 3D-MBD samples with QIAGEN's RNeasy (cat# 74134) using the protocol provided by the manufacturer. Quantity and purity of the extracted RNA samples was measured with a NanoDrop™ 2000 spectrophotometer. The RNA as converted to cDNA with Thermo Fisher's High-Capacity cDNA Reverse Transcription Kit (cat# 4368814) using the manufacturer's thermo cycler settings recommended for RT. The resulting cDNA concentration and purity was measured with a NanoDrop™ 2000 spectrophotometer. The cDNA samples were mixed with TaqMan® Fast Advanced Master Mix (cat# 4444557), the reaction solution was added to the prepared TaqMan® Gene Expression Assays 96-well Standard (0.2-mL) TaqMan® Array plates (cat# 4418741 and 4414100), and the

plates were run on a ViiA 7 Real-Time PCR system (Thermo Fisher).

2.37 Hydroxyapatite Content

Lonza's OsteoImage™ Mineralization assay was used to assess sample HA content. Spent medium was carefully removed from each well and saved for the CTX-1 ELISA assay. The wells were gently washed once with 1X DPBS and samples were fixed in 4% formaldehyde as previously described. After fixation, all samples were washed twice with 1X OsteoImage wash buffer and appropriately diluted Staining Reagent was added to each well as per the manufacturer's instructions. Plates were covered and incubated in the dark at room temperature for 30 minutes. After staining, the samples were washed three times with 1X OsteoImage Wash Buffer, leaving the buffer in the wells for five minutes per wash. After the final wash plates were read on a fluorescent plate reader (Biotek's Synergy H4) with excitation and emission set at 492/520 as recommended in the OsteoImage protocol. Plates were also viewed via fluorescent microscope (Nikon Eclipse Ti).

Data was processed in Excel and mean relative fluorescent values were transferred to GraphPad Prism 8 where dose response curves were generated using nonlinear regression curve fit with log (agonist or inhibitor) vs response -variable slope (four parameter).

2.38 Fourier Transfer Infrared Spectroscopy and Micro-CT

3D-NBF samples were fixed as previously described and maintained in 1X D-PBS. Prior to FTIR analysis the D-PBS was removed and samples were transferred to aluminum foil and dried in a lab oven at 45°C for 2 hours. The dried 3D-NBFs were made into a fine powder with a mortar and pestle and run on a Shimadzu IRSpirit. Hydroxyapatite powder (Sigma cat#702153) was run as an experimental control.

Fixed bone samples were samples were scanned at 90 kV, 100 µA and 9 µm voxel size using a Bruker Skyscan 1275 scanner with 1 mm aluminum filter. The images were reconstructed into a 3-D volume using NRecon (Bruker Corp., Billerica, MA).

2.39 Type I Collagen C-telopeptide (CTX-I) ELISA Assay

A CTX-1 ELISA assay (Chondrex, cat#6033) was run on all the spent media collected from the normal and MBD *in vitro* bone samples. Plates were prepared according to the manufacturer's instructions; capture antibody was added and plates were incubated overnight at 4°C. The next day a premixed solution consisting of 75 µl of each sample or standard or Solution B (blank) was added to 75 ul biotinylated CTX-1 was made and 100 ul of the mixture was added to the 100 µl capture antibody already in the well. Plates were covered and incubated for two hours at room temperature. Plates were washed three times with 1X wash buffer, including inverting and blotting them on clean absorbent towels after each wash. A streptavidin peroxidase solution was added to the empty wells at 100 µl/well and plates were covered and incubated for thirty minutes at room temperature. Plates were washed three times with 1X wash buffer, including inverting and blotting them on clean absorbent towels after each wash. Wells were not allowed to dry out between each step. A 3,3′,5,5′-Tetramethylbenzidine (TMB), peroxidase substrate, solution was added at 100 µl/well and plates were covered and incubated for twenty-five minutes at room temperature. A stop solution, consisting of 2N sulfuric acid was added to each well at 50 µl/well. Plates were read on a multi-mode plate reader/spectrophotometer (Biotek's Synergy H4) and the optical density (OD) values at 450 nM were captured. The resulting data were processed in Excel and sample CTX-1 content was quantified by comparing the sample and standards' OD450 values and back calculating sample

CTX-1. Dose response curves for samples derived from the respective therapeutic interventions were generated in GraphPad Prism 8 as previously described.

2.40 Therapeutic Intervention

The 3D-MBD samples were treated the following therapeutic agents: lenalidomide (Millipore Sigma, cat#901558), alendronate sodium (Millipore Sigma, cat# 126855), Anti-Sclerostin Antibody, clone 7B6.1 (Millipore Sigma, cat# MABS445), Anti-RANKL Antibody, clone 6A12.1 (Millipore Sigma, cat# MABS1696). Stock concentrations were made using manufacturer's instructions and all agents were administered at 2X concentration in the Complete Bone Medium supplemented with 0.2% DMSO added to an equal volume of medium. On days 4 and 8, media was removed from each well and replaced with Complete Bone Medium supplemented with 0.1% DMSO and each respective compound at the relevant concentration. On day 12, the spent media was collected from each well for use in the CTX-1 ELISA assay and samples were analyzed via OsteoImage Mineralization as previously described.

2.50 Statistical Analyses

2.51 Analysis of Taqman™/RT-PCR Data

The resulting data were processed, mean Ct was calculated, normalized to GAPDH, and 2-ΔΔCt values were generated, in Excel and relative quantification (RQ) heat maps were created in GraphPad Prism 8. Fold changes were determined by comparing RQ values for different samples/conditions.

2.52 Analysis of CTX-1 in Media from Complete Medium, Normal 3D Bone, and 3D-MBD

An ANOVA analysis of the three data sets was performed using GraphPad Prism 8.0 software and included p-values derived from Brown-Forsythe and Bartlett's test.

2.53 Analysis of OsteoImage and CTX-1 ELISA Data from Treated and Untreated 3D-MBD Samples

OsteoImage Assay data was reported as relative fluorescence units (RFU) excitation/emission wavelengths (492/520). CTX-1 content was back calculated from the standard curve provided with ELISA kit. Untreated diseased bone (negative) and normal bone (positive) controls were used to gauge the effectiveness of the therapeutic intervention on the bone samples. All data were processed in GraphPad Prism 8.0 and dose response curves were generated using nonlinear regression curve fit with log (agonist or inhibitor) vs response - variable slope (four parameter). Multiple t-tests comparing untreated 3D-MBD to various treatments on 3D-MBD was performed using the two-stage linear step-up procedure of Benjamini, Krieger and Yekutieli, with Q = 1%. Each row was analyzed individually, without assuming a consistent SD.

Results

3.1 BMSC Osteogenic Differentiation, Osteoblastogenesis, and ECM Mineralization

The growth, osteogenic differentiation, and mineralization of Matrigel-embedded HBMSCs were kinetically monitored by light microscopy using an Incucyte (Essen Bioscience). The increased opacity of mineralization zones obscures the cellularity of the bone-like fragment. The area of each mineralization zones increases until they combine over a 34-day period forming the complete 3D Normal Bone-like Fragment (3D-NBF) (Figure 5A). The ossified product of the osteogenically-differentiated BMSCs was visible to the unaided eye after 28 days in culture (Figure 5B). The Incucyte's measurement tool was used to assess 3D-NBF average diameter, 2.43 mm, and diameter standard deviation, 13.8%.

A

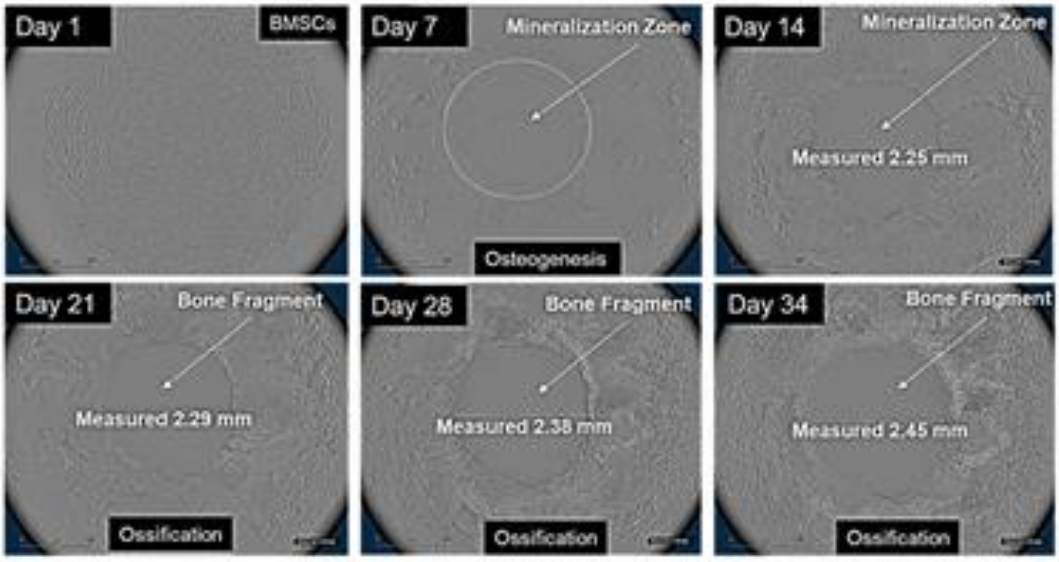

B C

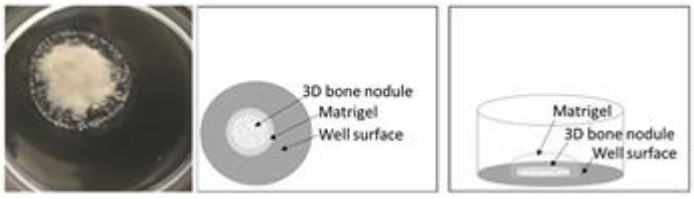

Figure 5. Growth, Differentiation, and Mineralization of BMSCs. Matrigel-embedded human BMSCs grown in the presence of osteogenic differentiation media (OsteoMax-XF™) become functional osteoclasts that secrete osteoid and HA that forms a mineralized bone micro-fragment of approximately 2.45 mm in diameter.

3.2 3D-NBF Characterization

3.21 Alkaline Phosphatase Staining

Osteogenic differentiation of the human BMSCs into osteoblasts was monitored every seven days by alkaline phosphatase (AP) staining (Figure 6A). Skeletal AP is anchored to inositol-phosphate on the cell membrane of functional osteoblasts and is a key osteogenic biomarker. AP catalyzes BCIP (5-Bromo-4-chloro-3-indolyl phosphate) and further reacts with NBT (nitro blue tetrazolium), producing a dark insoluble formazon precipitate, diformazan [57]. The alkaline phosphatase staining of the 3D-NBFs produced by osteogenically-differentiated BMSCs (BMSC+) were compared to control cell lines maintained in the presence of OsteoMax-XF including, cell-free Matrigel (M+), HEK-293 cells (HEK293+), and Caco2 cells (Caco2+). AP staining was also performed on BMSCs grown in stem cell media to serve as a negative control (BMSC-). The diformazan was localized in the mineralized regions of the 3D-NBFs and in the cytoplasm of Caco2 cells [58]. The AP staining intensity increased in the 3D-NBFs over time until it reached maximum opacity at day 28 and beyond (Figure 6B).

A

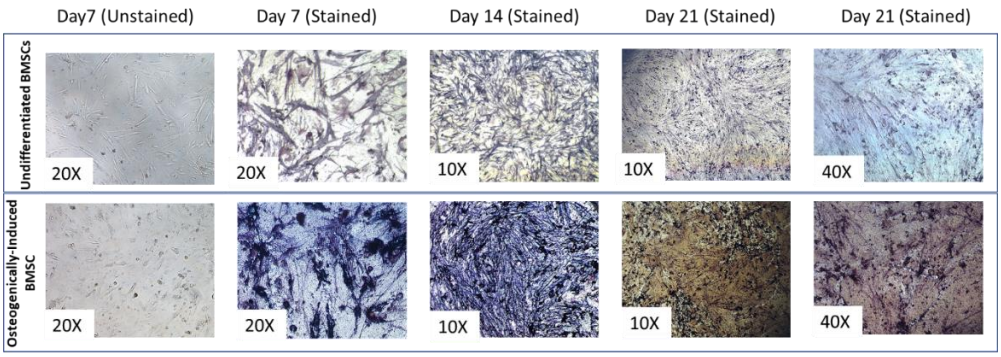

B

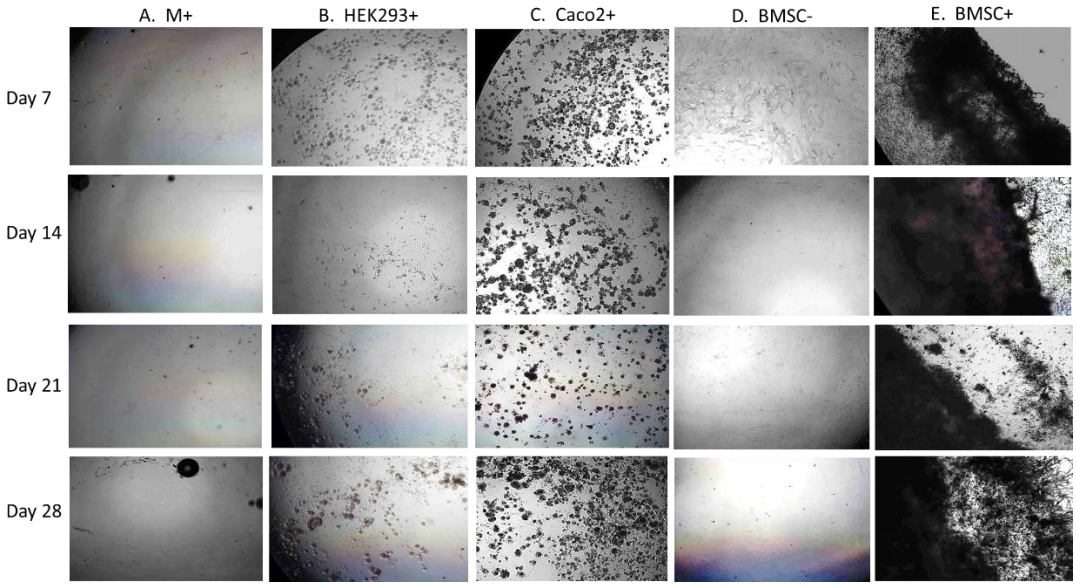

Figure 6. Alkaline Phosphatase Staining of Human BMSC-Derived Osteoblasts. A. Alkaline Phosphatase Staining of hBMSCs grown in StemPro™ (non-osteogenic) and OsteoMaxXF™ (osteogenic differentiation) media. Human BMSCs grown in OsteoMax XF for seven days generate a dark blue-purple when exposed to NBT/BCIP, a substrate of alkaline phosphatase. B. BMSC+ wells show a dark precipitate in the mineralized region of the 3D-NBFs. Caco2 cells have reported AP activity and show cell-based staining pattern while other controls appear negative.

3.22 Alizarin Red S Staining

Osteogenic differentiation of human BMSCs into osteoblasts was characterized for calcium deposition through staining with Alizarin Red S (ARS), an anthraquinone dye that binds

calcium [59]. In aqueous solution, ARS and Ca2+ ions precipitate to form brick-red deposits (Figure 7A). ARS accumulated in the mineralized 3D-NBFs and appeared as deep red deposits in the bone-like tissue, while little to no staining was observed in any of the control wells (Figure 7B). Like AP, 3D-NBF ARS staining increased in intensity as the mineralization process progressed demonstrating peak calcium deposition at Day 28 and beyond.

A

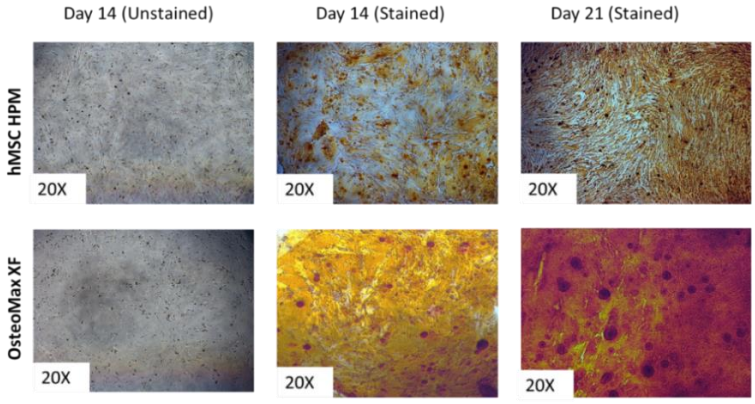

B

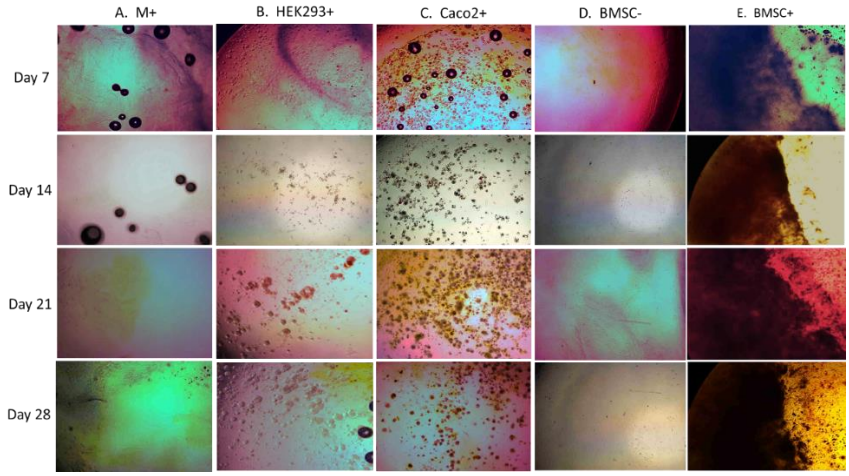

Figure 7. Alizarin Red S Staining of Human BMSC-Derived Osteoblasts. A. The number of calcium deposits increase with prolonged culture in osteogenic differentiation medium. By Day 21 deep-red deposits permeate the mineralized bone micro-fragment. B. While little to no staining was observed in the M+, BMSC-, and control cell lines, dark red staining was present in the BMSC+ sample wells, especially in the 3D-NBFs.

3.23 Osteogenic Gene Expression of BMSCs, Primary OBs, and 3D-NBFs

RNA isolated from BMSCs, primary human osteoblasts (PHO) and 3D-NBFs was screened for transcript expression of over ninety osteogenic markers. Genes associated with bone extracellular bone matrix (collagen, SPARC, and MMP2) and alkaline phosphatase (ALPL) were comparable between PHO and the normal *in vitro* 3D bone micro-fragments and downregulated in the MBD model (Figure 8). Gene expression was normalized with the housekeeper values (GAPDH) for each sample and relative quantification (RQ) was determined (Figure 8). Type 1 collagen transcript levels greatly increased over 1,000-fold in 3D-NBF samples over the original BMSCs. The same trend appeared in collagen type 1 alpha 2 and collagen type 3 alpha 1 chain transcripts. Osteonectin, a calcium-binding glycoprotein secreted by OBs during bone formation [60] was also upregulated greater than 1,000-fold in the 3D-NBF and PHO samples. ANOVA analysis of these highly expressed osteoblastic genes generated a p value of 0.0125. Osteopontin, an osteoclast anchoring protein secreted by OBs, was highest in the OC-containing 3D-NBF culture (>150-fold higher than the BMSC and 14-fold higher than primary OBs). Another osteogenic marker, osteocalcin, a hormone secreted by osteoblasts that regulates metabolic activity [15], was approximately 10-fold higher in the 3D-NBF samples and primary OB samples when compared to levels found in BMSCs (Figure 8). ANOVA analysis of these moderate/lowly expressed osteoblastic genes generated a p value of 0.2017.

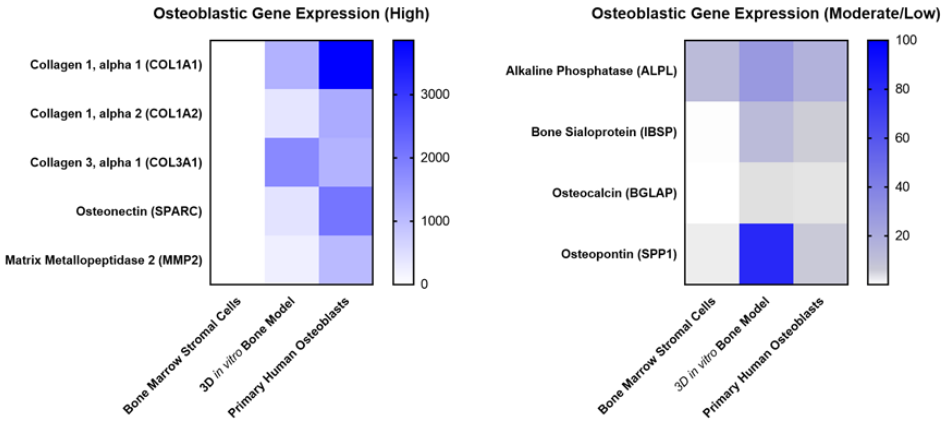

Figure 8. Osteogenic Gene Expression Profiling of BMSCs, PHOs, and 3D-NBFs. Several osteogenic genes were upregulated in the 3D in vitro bone model (3D-NBF samples) like collagen type 1, osteonectin, alkaline phosphatase, bone sialoprotein, osteocalcin and osteopontin. Normalized gene expression relative quantification (RQ) values show that gene expression in the 3D-NBFs is similar to that observed in PHOs.

3.24 Actin Distribution/Phalloidin Staining and Multinucleation

Since human BMSCs, osteoblasts, and osteoclasts differ morphologically, a Phalloidin-AlexaFluor488 (green) stain was used to visualize the actin distribution in each cell type in the model of MBD (Figure 9). DAPI, a nuclear counterstain, was used to identify multinucleated cells.

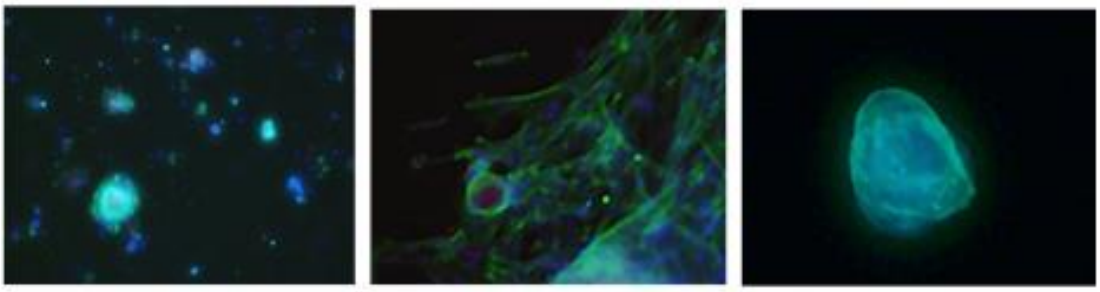

Figure 9. Microscopic Morphological Identification of Osteoclasts. Actin distribution of the 3D-NBF samples depicts large multinucleated with an actin rich periphery resembling the osteoclastic podosomal belt. In contrast, actin distribution in BMSCs and osteoblasts appears linear and somewhat filamentous throughout the cell's cytoplasm. Monocytic fusion leads to formation of the osteoclast with a roughly five times larger diameter than the osteoblast.

3.25 Fourier Transfer Infrared Spectroscopy and Micro-CT Analysis of 3D-NBFs

The 3D-NBF samples were analyzed via Fourier Transfer Infrared Spectroscopy (FTIR) to monitor HA and collagen composition. FTIR is a widely accepted manner of a assessing bone composition [61, 62]. The 3D-NBF FTIR spectrum contains corresponding peaks for HA, all valences, and collagen (Figure 10A). HA valence peaks at approximately 550 cm^{-1} and 1,100 cm^{-1} matched those found in HA powder (Figure 10B).

A diagram depicting the slide containing the 3D-NBF in Matrigel (Figure 10C) shows how the samples were analyzed via micro computed tomography (micro-CT), an imaging technique that utilizes x-rays to create a high resolution image of 3D objects. Micro-CT analysis, a technique used to study bone mineralization [63], of the 3D-NBF revealed a uniform pattern of mineralization throughout the sample (Figure 10D).

A B

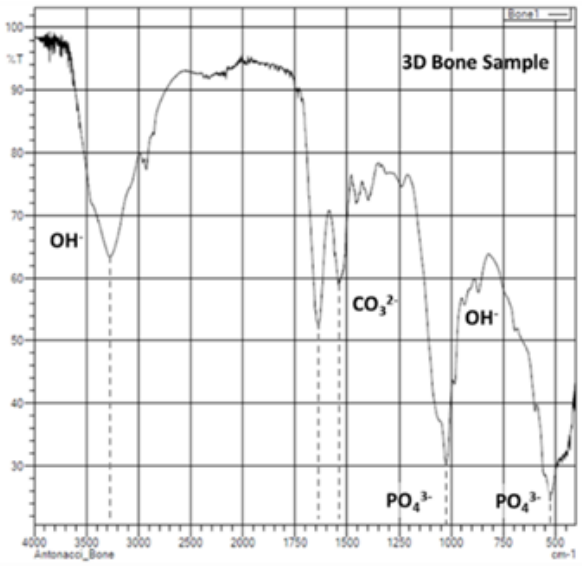

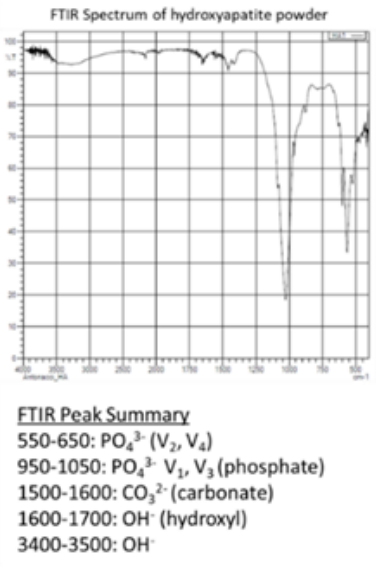

C D

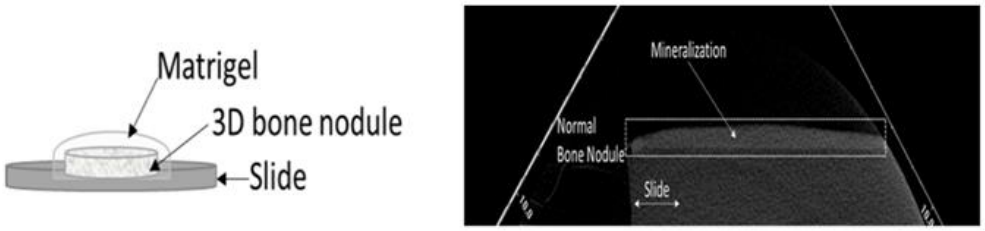

Figure 10. FTIR and Micro-CT Analysis of 3D-NBFs. A. The FTIR spectrum of bone-like fragments derived from the BMSC+ culture contains the prominent and expected HA-associated peaks at roughly 500 and 1050 cm-1, comparable to that of HA powder and the collagen-related amide peaks at roughly 1550 and 1650 cm-1 found in mammalian bone (not shown). C. Lateral diagram showing the location of the sample with respect to the surface of the slide. D. Micro-CT analysis of a 3D-NBF with a relatively uniform mineralization pattern across the entire length of the sample.

3.26 Hydroxyapatite Content of 3D-NBFs and Control Samples

Lonza's OsteoImage assay contains a proprietary agent that binds directly to HA and can be analyzed quantitatively by using a plate reader set to 492nm excitation and 520nm emission wavelengths (Figure 11A) or qualitatively through fluorescent microscopy (Figure 11B). The 3D-NBFs formed by the osteogenically-differentiated BMSCs contained increasing amount of HA over time (Figure 11). Statistical analysis (ANOVA) of the RFU values resulting from different culture conditions generated a p value of 0.0109. The staining was localized in HA-rich areas of 3D-NBFs and peripheral OBs resulting in a bright green staining pattern with little to no background staining in the rest of the well (Figure 11B). While some background HA staining was detected in the M+ wells it did not resemble the mineralized 3D-NBF and little to no fluorescence was detected in other control wells (Figure 11B).

A

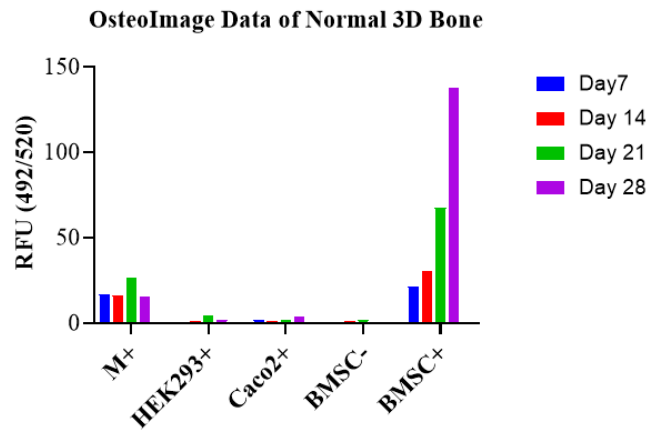

B

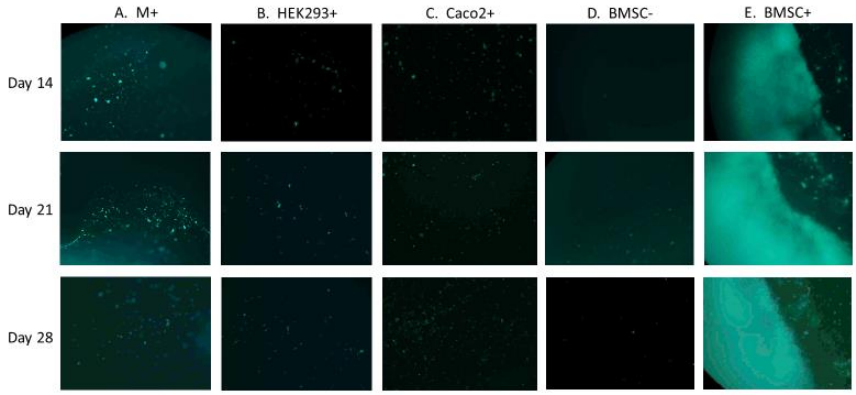

Figure 11. Hydroxyapatite Content of 3D-NBFs and Control Samples. A. Weekly RFU values for BMSC+ (3D-NBF) and controls Day 7 through Day 28. Fluorescent photomicrographs of the BMSC+ (3D-NBF) and control wells at 14, 21, and 28 days in culture.

3.3 Characterization of 3D-MBD Model

3.31 Osteogenic Gene Expression Profiling of 3D-NBF and 3D-MBD Samples

3D-NBF and 3D-MBD RNA samples were evaluated for osteogenic gene transcript levels via RT-PCR. Decreased expression of alkaline phosphatase (-3.00-fold, p=0.0214), osteonectin (-16.22-fold, p<0.001)), and type 1 collagen (-15.09-fold, p=0.0078) was observed in

the 3D-NBF samples (Figure 12) confirming the well-documented suppressive effect of MM on bone formation [64, 65]. BMP6, the only bone morphogenetic protein secreted by myeloma cells, expression increased (30-fold, p=0.0014). Several publications reported high levels of BMP6 in MM patient BM aspirates and revealed that its antiproliferative effect on myeloma cells is associated with improved MM prognosis [66, 67, 68].

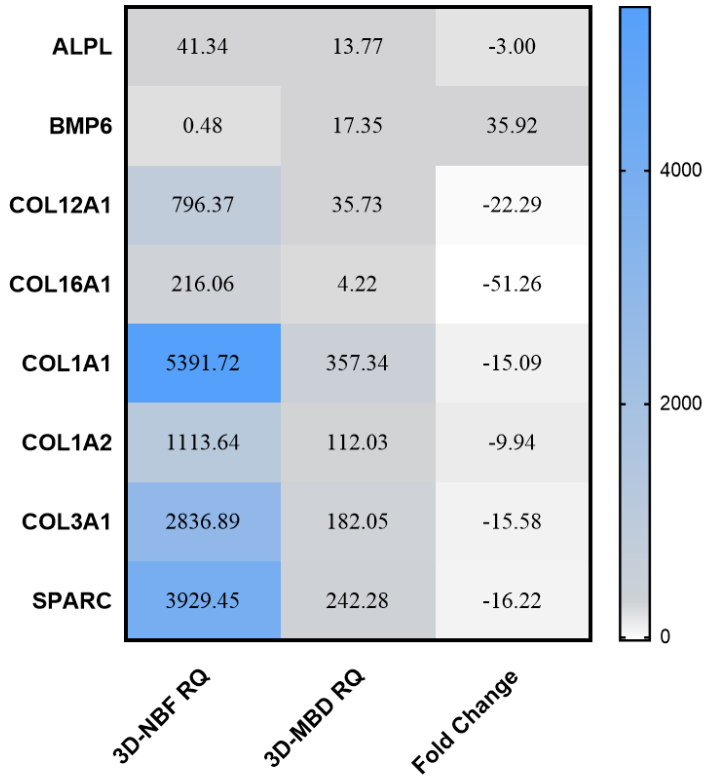

Figure 12. Osteogenic Gene Expression in 3D-NBF and 3D-MBD Samples. Osteogenic gene expression was determined for 3D-NBF and 3D-MBD samples (n=3). Transcript levels were normalized to GAPDH and Relative Quantification (RQ) values were determined for each sample using $2^{-\Delta\Delta Ct}$. Fold change was determined for both upregulated and downregulated genes in MM-induced MBD samples with respect to those obtained from the 3D normal bone fragments. A statistical analysis (t-test) was performed and p values for reported target genes were <0.05 (six of them were <0.01).

3.32 Quantified HA and CTX-1 Content in Normal and MBD Bone Micro-fragments.

A model of human MBD was created by co-culturing the normal *in vitro* bone model with four different MM-derived plasmacytomas (MM1S, RPMI-8226, H929, and U266) respectively at four fixed cell densities. After twelve days of exposure the MBD model was monitored for changes in bone mineralization (HA content) and resorption (CTX-1). HA content was quantified through Lonza's OsteoImage Assay (Figure 13) and liberated CTX-1 was measured by Chondrex's ELISA assay kit (Figure 14). HA content dropped in 3D-NBF samples cultured in the presence of MM.1S, RPMI 8226, H929, and U266 cells for 12 days with respective decreases of 1.23 to 1.39-fold, 2.21 to 4.05-fold, 2.51 to 5-fold, and 1.89 to 4.24-fold in total HA content (Figure 13). A statistical analysis (ANOVA) was performed on the MM cell concentration-dependent decrease in HA ($p<0.001$). The same MM-subjected culture conditions liberated CTX-1 in the media of each 3D-NBF sample with respect to MM cell line present in the culture (MM.1S: 2.25 to 87.74-fold, RPMI 8226: 1.95 to 50-fold, H929: 2.2 to 83.31-fold, and U266: 2.03 to 50.44, Figure 14). A statistical analysis (ANOVA) revealed significant MM cell concentration-mediated increases in CTX-1 ($p=0.0068$).

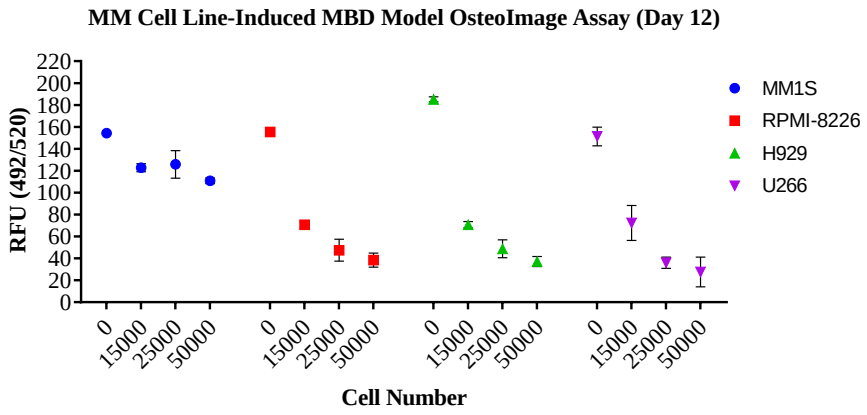

Figure 13. HA Content of Human 3D-NBF Exposed to MM Cells. A plasmacytoma cell concentration-dependent decrease in HA content was observed in all MM-exposed bone micro-fragments after twelve days (n=3). Unexposed HA content remained consistent (n=3).

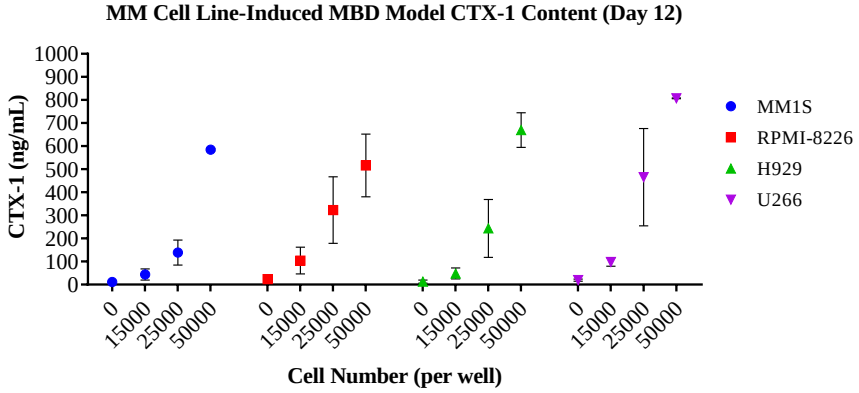

Figure 14. Liberated CTX-1 Levels in Human 3D-NBFs Exposed to MM. Increased CTX-1 values were observed in human bone micro-fragments exposed to higher cell numbers of human plasmacytoma cell lines (n=3). Media derived from normal unexposed bone micro-fragments contained trace amounts of CTX-1 (n=3).

3.33 Micro-CT Analysis of 3D-MBD Samples

RPMI 8226-induced 3D-MBD bone-like fragments were analyzed via micro-CT and compared to images generated from 3D-NBF samples. Large voids in the mineralized regions of the tissue appeared in the 3D-MBD sample (Figure 15A). This loss of mineralized tissue could be due to processing, but the 3D-NBF and 3D-MBD samples were fixed, washed, and collected simultaneously with the same protocol. Although the MM-induced loss of HA content and elevated CTX-1 found in these samples (Figures 13 and 14) could be responsible for diminished structural integrity, additional supporting data, like bone volume and surface density, were not measured. Diagrams of the 3D-NBF and 3D-MBD models were created to assist in visualizing changes in mineralization zones within the normal and diseased samples (Figure 15B).

A

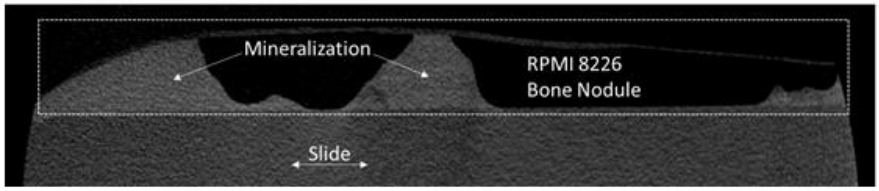

B

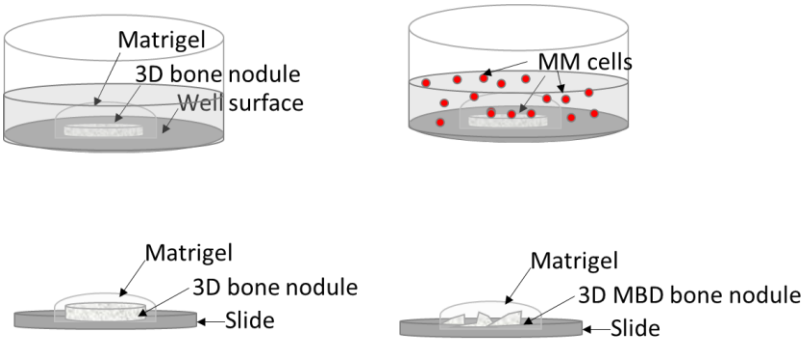

Figure 15. Micro-CT Analysis of 3D-MBD Samples. A. Micro-CT generated image of the RPMI 8226-exposed 3D-NBF sample shows voids in the bone-like tissue. B. A diagram of the 3D-NBF and 3D-MBD models.

3.34 CTX-1 Analysis of 3D-NBF and RPMI-8226-Induced 3D-MBD

CTX-1 levels were compared in the complete bone medium, 3D-NBF, and 3D-MBD models. 3D-MBD samples were cultured in the presence of 20,000 RPMI 8226 cells for twelve days. An approximately 10-fold increase in CTX-1 was detected in the 3D-MBD media samples compared to those collected from the 3D-NBF model (Figure 16A). Average free CTX-1 levels were: complete medium: 9.34 +/-0.46, normal 3D bone (3D-NBD): 57.91 +/- 18.23, and RPMI 8226-induced MBD: 598.04 +/- 83.41. Statistical analysis (ANOVA) of the CTX-1 values in each sample group generated a p-value <0.001 (Figure 16A). Light microscopy pictures captured morphological differences in the 3D bone-like samples; the 3D-NBFs appeared quite opaque while the 3D-MBD samples contained regions of increased translucence (Figures 16B and 16C).

A

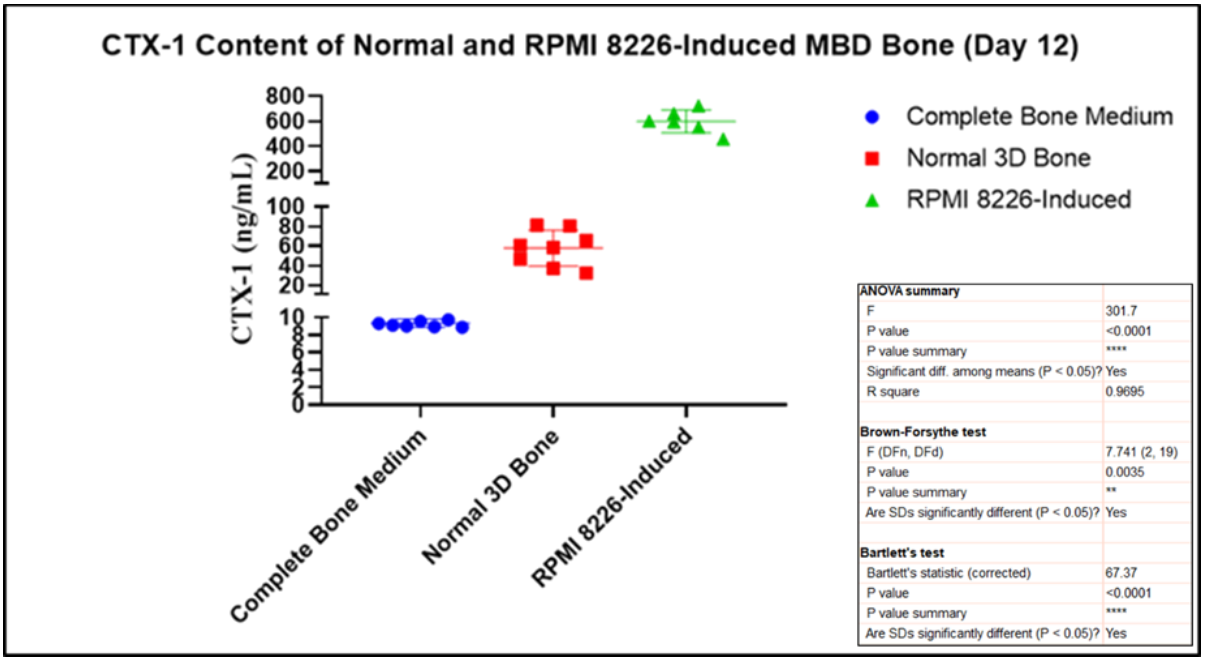

B C

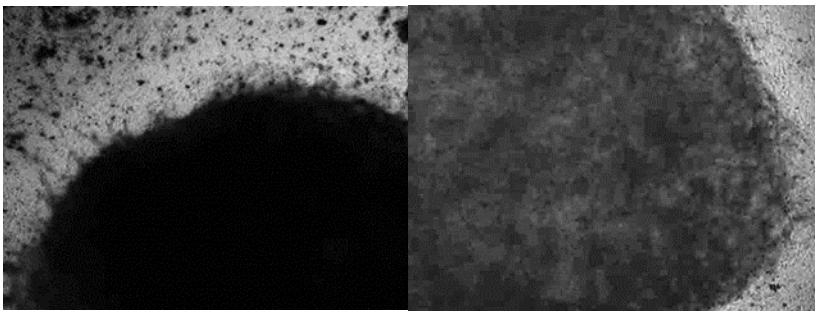

Figure 16. CTX-1 Analysis of 3D-NBF and RPMI 8226-Induced 3D-MBD Samples.

A. CTX-1 content of the complete medium, normal 3D bone fragments (3D-NBF), and 3D-NBF samples cultured in the presence of RPMI-8226 for twelve days was measured (3D-MBD). B. Brightfield microscopic image of a 3D-NBD. C. Brightfield microscopic image of a 3D-MBD.

3.4 Assessment of Therapeutic Intervention on 3D-MBD Samples

RPMI 8226-induced 3D-NBF samples were treated with several different therapeutic agents including: an immunomodulatory drug (lenalidomide), a bisphosphonate (alendronate), and two separate biotherapeutic agents/monoclonal antibodies, anti-Dkk1 and anti-sclerostin.

HA was measured on treated samples, normal 3D-NBF and untreated 3D-MBD controls (Figure 17). The RPMI 8226-induced myeloma bone disease bone-like fragments treated with individual therapeutic agents had sizeable increases in detectable HA present in the OsteoImage™ assay: alendronate (2.6-fold, p=0.13), lenalidomide (3.4 fold, p=0.007), anti-sclerostin (3.7, p=0.004), anti-DKK1 (7-fold, p=0.002). Simultaneous administration of all aforementioned treatments lead to a roughly 5-fold increase (p=0.002) in HA while all of the agents minus alendronate lead to a 6-fold increase (p=0.016) in HA content (Figure 17A). Corresponding images for 3D-MBD samples treated with the all of the therapeutic agents reveals the relative fluorescence as indicated by the OsteoImage™ assays fluorescently-labeled HA-binding reagent (Figure 17B). Nonfluorescent regions of 3D-MBD samples treated with lower concentrations of the therapeutic agents were identified and matched those observed in previous experiments.

A

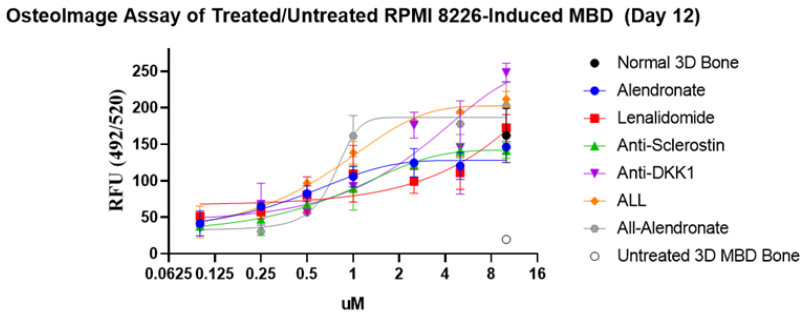

B

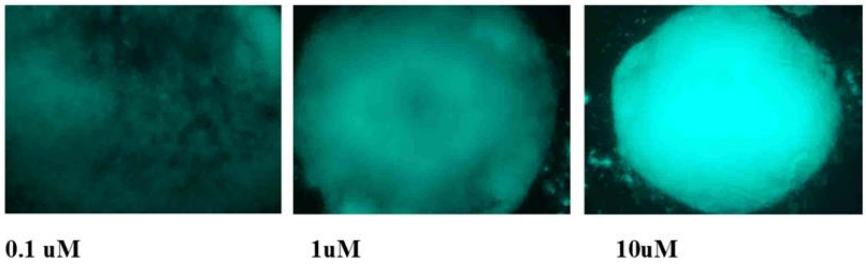

Figure 17. The Effect of Different Therapeutic Agents on 3D-MBD HA Content. A. Dose-dependent increases in HA content were observed in treated RPMI 8226-induced 3D-MBD bone-like fragments. The submicromolar EC_{50s} demonstrate the potent nature of the combinatorial treatment to restore bone mineralization (n=3). B. Fluorescent microscopy reveals HA content in 3D-MBD samples treated with the battery of therapeutic agents at 0.1, 1, and 10 μM respectively.

CTX-1 content was measured in the media samples collected from the treated 3D-MBD, untreated 3D-MBD and 3D-NBF control wells (Figure 18). Dose-dependent decreases in CTX-1 were observed in 3D-MBD samples with individual therapeutic agents for twelve days, with maximum reductions detected at the 10 μM concentrations: alendronate (21-fold, p=0.003), lenalidomide (7-fold, p=0.003), anti-sclerostin (23-fold, p=0.003), anti-DKK1 (21-fold, p=0.003). Combining the anti-MM drug and bone-modifying agents proved even more effective at inhibiting bone resorption. Sizeable decreases in CTX-1 present in the media after twelve days of treatment were noted for all of the agents (35-fold, p=0.003) and all of the agents minus alendronate (24-fold, p=0.003) (Figure 12C). Statistical analysis (t-test) of the treated 3D-MBD CTX-1 generated a p-value of 0.002. Nonlinear regression analysis of the CTX-1 ELISA data derived from the combined therapies generated left-shifted, more potent, IC_{50} values than individual treatments.

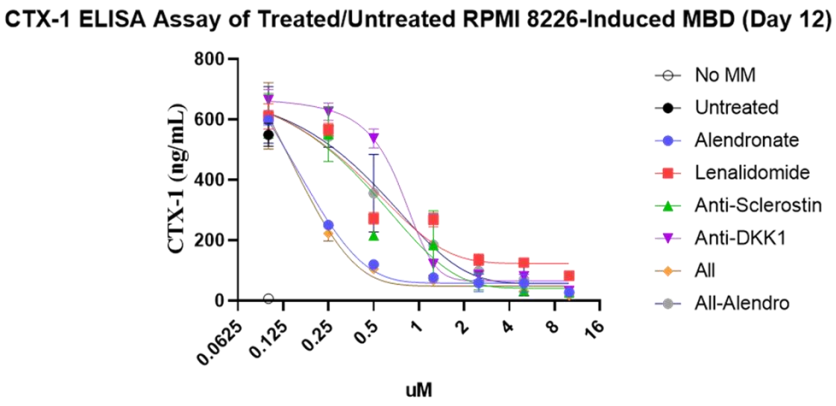

Figure 18. The Effect of Different Therapeutic Agents on 3D-MBD CTX-1 Levels. A dose-dependent decrease in liberated CTX-1 was detected in supernatants from MBD bone micro-

fragments exposed to each respective plasmacytoma (n=3). The combinatorial treatment had no effect on the CTX-1 levels in the supernatant of untreated/normal *in vitro* bone.

Conclusion

A three-dimensional normal bone-like fragment was created through the osteogenic differentiation of human BMSCs into osteoblasts capable of mineralizing the osteoid-like ECM and producing an ossified product. A thorough analysis of the 3D-NBFs revealed high levels of alkaline phosphatase activity, large calcium deposits, increased expression osteogenic transcripts, enriched HA content with the requisite corresponding HA and collagen FTIR peaks, and uniformly dense mineralization patterns.

Bone formation in the 3D-NBF system resembles intramembranous ossification. Osteoblasts deposit calcium into a collagen-rich ECM, similar in composition to the endosteal niche, and form a mineralized bone fragment. The addition and subsequent osteoclastogenic induction of BMMs create a functional and somewhat homeostatic replica of the bone remodeling process. It is a chondrocyte-free system that generates normal compact spongy bone-like fragments, similar to trabecular bone, developed directly from sheets of Matrigel™-embedded BMSC-derived connective tissue. Since Matrigel™ is a gelatinous protein mixture secreted by Engelbreth-Holm-Swarm (EHS) mouse sarcoma, other more bone-like ECMs should be explored to enhance ossification and mineralization. These could include direct bone-derived biomatrices and inert synthetic hydrogels enriched with factors that promote osteogenic differentiation.

Others have developed, deployed, and published data from BMSC-derived *in vitro* bone models [69, 70], but they were designed for use in bone graft implantation and did not include the resorptive component of bone. Jaquiéry et al. noted the osteogenic potential of BMSCs, highlighting increased osteogenic gene expression, enhanced AP activity and superior calcium deposition, over jaw periosteal cells (JPC) as potential *in vitro* sources of bone formation. Some

recently published review articles recognize the potential of *in vitro* models of bone remodeling, but a functional semi-homeostatic 3D model of human skeletal remodeling had yet to be established [71, 72]. Lopa et al. were able to create a vascularized 3D model of bone remodeling replete with OB and OC precursors and Human Umbilical Vein Endothelial Cells (HUVEC), but it was created to study bone cell-endothelial crosstalk and lacked functional longevity because OB and OC precursors were added and differentiated simultaneously [73]. The model described in this study was able to incorporate and maintain osteoclastic resorption for several weeks by adding BMM as osteoclast precursors post 3D-NBF formation, addressing the relatively short-lived nature of primary osteoclasts [51].

Introduction and subsequent osteoclastogenic differentiation of BMMs elicited monocytic fusion and formation of functional osteoclasts. Microscopic analysis revealed several multinucleated cells with an actin-rich podosomal belt, common morphological attributes of osteoclasts. The resorptive capability of this 3D *in vitro* bone model was examined through changes in free CTX-1 in the media post introduction of MM cells known to promote osteoclastogenesis and osteoclastic resorption.

Thorough characterization of this replica of the human bone remodeling process confirmed robust osteogenic BMSC differentiation into functional bone-forming osteoblasts and the bone-like attributes of their mineralized product, as well as osteogenic BMM differentiation into functional bone-resorbing osteoclasts and liberation of collagen C-terminal telopeptide. The Media from the 3D-NBFs had a five to six-fold increase in CTX-1 content over the cell-free complete differentiation medium control, but the introduction of a myeloma cells to the 3D-NBF samples would cause a roughly ten-fold increase in CTX-1 release over the 3D-NBF values.

A three-dimensional microphysiological model of human myeloma disease was created through the incorporation of RPMI 8226, a human myeloma-derived cell line, to the previously formed 3D-NBFs. The introduction of the MM cell line disrupted the normal bone remodeling process by simultaneously suppressing bone formation, as evidenced by the loss in HA content and intensified resorption, demonstrated by a substantial increase in free CTX-1. This result coincided with decreased integrity observed via micro-CT analysis of 3D-MBD fragments as compared to the 3D-NBFs.

While others created models that simulate the interaction between MM and the bone marrow stroma and its impact on bone formation, the complete 3D model of simultaneous osteoblastic bone formation and osteoclastic resorption had yet to be created and used to assess the effect of MM therapeutic intervention on MBD [74, 75]. Belloni et al. monitored the effects of MM therapeutic agents on MM-stromal interactions, but the *in vitro* bone model used in the study lacked functional osteoclasts [75].

Murine models of myeloma bone disease were developed at the turn of the 21st century [76] and improved models were recently published [77]. While these *in vivo* systems are helpful in assessing drug efficacy and in investigating toxicological liabilities, the interspecies discordance is of concern. The use of humanized mouse model contains a physiological integration of human and mouse properties into a single functional bone tissue while maintain species-specific structural differences [78]. These murine systems do not annul the need for functional human systems of skeletal remodeling especially when studying therapeutic intervention of myeloma bone disease and both should be used synergistically to conduct preclinical assessments of potential MBD treatments.

The MM-compromised bone-like fragments generated in this study were used to evaluate the efficacy of both individual and combinatorial therapies on restoring HA and CTX-1 to levels observed prior to myeloma cell line addition. Combinatorial treatment with an immunomodulatory drug and three bone modifying agents, including alendronate, anti-sclerostin, and anti-DKK1 proved most effective at enhancing bone formation while suppressing resorption. The treated 3D-MBD fragments displayed higher HA levels and lower CTX-l levels than their untreated counterparts, highlighting the restorative nature of the treatment. The effectiveness of the therapy appeared to be dose-dependent where higher concentrations of drugs correlated with higher HA composition and inversely-correlated with lower CTX-1 found in the media. Fluorescent microscopy of the fluorescently-labeled HA binding protein in the treated and untreated 3D-MBDs confirmed the robust nature of HA content in treated samples and revealed mixed patterns of HA content throughout the untreated samples.

Additional micro-CT analyses are required to fully establish the bone volume and surface density of 3D-NBF and 3D-MBD samples. They would also help identify osteolytic lesion in the 3D-MBD bone-like fragments, assess the loss of structural integrity in the myeloma bone disease model with respect to the normal 3D-NBF, and evaluate the restorative nature of therapeutic agents on the 3D-MBDs post treatment. Histological analysis of fixed sections derived from these samples could also have an added value in assessing the impact of the MM on bone integrity.

While IMiDs, like lenalidomide, are effective at eliciting proteasomal degradation of essential transcription factors and suppress MM proliferation and survival, their role in reestablishing normal bone remodeling is unclear. Coupling standard of care MM treatments with osteoclast apoptosis inducing bisphosphonates, like alendronate, and other bone modifying

agents is quite encouraging. Future evaluations should include other standard of care treatments like the proteasome inhibitor, bortezomib and other inhibitors of bone resorption, like the promising anti-RANKL antibody, denosumab. Effective therapeutic interventions should address the various molecular signaling mechanisms by which MM wreaks havoc on the bone marrow niche and restore the unencumbered osteogenic potential of BMSCs while promoting balanced BMM osteoclastogenesis and bone metabolism (Figure 2).

This model of MM-disrupted skeletal remodeling also highlights the importance of targeting WNT inhibitors, like sclerostin and Dkk1, when treating MBD [79, 80]. Combinatorial treatment regimens are widely used in treating cancer, but incorporating novel bone modifying agents in relapsed refractory multiple myeloma could have a restorative effect on bone integrity and reveal the role of canonical WNT signaling in IMiD-resistance [27, 81]. This MBD model is capable of exploring the role of WNT signaling in MM-BM stromal interactions, determining potential treatments that suppress MM growth and survival while determining the therapeutic effect on bone health. Amgen's romosozumab is currently approved for use in osteoporosis, as is their anti-RANKL antibody, denosumab. Studies monitoring clinical efficacy of these bone modifying agents to treat MM have recently been published [82], combinatorial treatment regimens have yet to reach their full potential [83].

While no *in vitro* model of human bone physiology can precisely simulate the complex bone metabolism microenvironment, this 3D microphysiological model of MM-induced disrupted skeletal remodeling may serve as a biologically functional surrogate. It's amenable to high throughput screening of novel pharmacological bone-targeting agents while avoiding potential toxicological liabilities and interspecies discordance observed in *in vivo* studies of mammalian skeletal remodeling in lower species. The thorough characterization performed in

this thesis suggests that this replica of human osteogenic function should be translatable, but further studies are required to validate the untapped potential of this system.

References

1. Crockett JC1, Rogers MJ, Coxon FP, Hocking LJ, Helfrich MH. Bone remodeling at a glance. J Cell Sci. 2011 Apr 1;124(Pt 7):991-8. doi: 10.1242/jcs.063032.

2. Raggatt LJ, Partridge NC. Cellular and molecular mechanisms of bone remodeling. J Biol Chem. 2010;285(33):25103–25108. doi:10.1074/jbc.R109.041087.

3. Badawy T, Kyumoto-Nakamura Y, Uehara N, Zhang J, Sonoda S, Hiura H, Yamaza T, Kukita A, Kukita T. Osteoblast lineage-specific cell-surface antigen (A7) regulates osteoclast recruitment and calcification during bone remodeling. Lab Invest. 2019 Jun;99(6):866-884. doi: 10.1038/s41374-018-0179-4. Epub 2019 Feb 11.

4. Kim, J.H. and N. Kim, Signaling Pathways in Osteoclast Differentiation. Chonnam Med J, 2016. 52(1): p. 12-7.

5. Delaisse, J.M., The reversal phase of the bone-remodeling cycle: cellular prerequisites for coupling resorption and formation. Bonekey Rep, 2014. 3: p. 561.

6. Dodds, R.A., et al., Human osteoclast cathepsin K is processed intracellularly prior to attachment and bone resorption. J Bone Miner Res, 2001. 16(3): p. 478-86.

7. Parra-Torres, A.Y., et al., Molecular Aspects of Bone Remodeling, in Topics in Osteoporosis, M.V. Flores, Editor. 2013, IntechOpen: Rijeka.

8. Stamos, J.L. and W.I. Weis, The β-Catenin Destruction Complex, in Cold Spring Harb Perspect Biol. 2013.

9. Knight MN, Karuppaiah K, Lowe M, et al. R-spondin-2 is a Wnt agonist that regulates osteoblast activity and bone mass. Bone Res. 2018;6:24. Published 2018 Aug 14. doi:10.1038/s41413-018-0026-7

10. Xu X, Zheng L, Yuan Q, et al. Transforming growth factor-β in stem cells and tissue homeostasis. Bone Res. 2018;6:2. Published 2018 Jan 31. doi:10.1038/s41413-017-0005-4

11. Hill CS. Transcriptional Control by the SMADs. Cold Spring Harb Perspect Biol. 2016;8(10):a022079. Published 2016 Oct 3. doi:10.1101/cshperspect.a022079

12. Chen, G., C. Deng, and Y.P. Li, TGF-beta and BMP signaling in osteoblast differentiation and bone formation. Int J Biol Sci, 2012. 8(2): p. 272-88.

13. Rodríguez-Carballo E1, Gámez B2, Ventura F2. p38 MAPK Signaling in Osteoblast Differentiation. Front Cell Dev Biol. 2016 May 6;4:40. doi: 10.3389/fcell.2016.00040. eCollection 2016.

14. Li Y, Zhang W, Ren F, Guo H. Activation of TGF-β Canonical and Noncanonical Signaling in Bovine Lactoferrin-Induced Osteogenic Activity of C3H10T1/2 Mesenchymal Stem Cells. Int J Mol Sci. 2019;20(12):2880. Published 2019 Jun 13. doi:10.3390/ijms20122880.

15. Florencio-Silva, R., et al. (2015). "Biology of Bone Tissue: Structure, Function, and Factors That Influence Bone Cells." Biomed Res Int 2015: 421746.

16. Recker, R. R., et al. (2009). "Comparative effects of teriparatide and strontium ranelate on bone biopsies and biochemical markers of bone turnover in postmenopausal women with osteoporosis." J Bone Miner Res 24(8): 1358-1368.

17. Blair HC, Larrouture QC, Li Y, et al. Osteoblast Differentiation and Bone Matrix Formation In Vivo and In Vitro. Tissue Eng Part B Rev. 2017;23(3):268–280. doi:10.1089/ten.TEB.2016.0454

18. Orimo, H. (2010). "The mechanism of mineralization and the role of alkaline phosphatase in health and disease." J Nippon Med Sch 77(1): 4-12.

19. Kazandjian, D. (2016). "Multiple myeloma epidemiology and survival: A unique malignancy." Semin Oncol 43(6): 676-681.

20. Hameed, A., et al. (2014). "Bone disease in multiple myeloma: pathophysiology and management." Cancer Growth Metastasis 7: 33-42.

21. Weber, D. M., et al. (2007). "Lenalidomide plus dexamethasone for relapsed multiple myeloma in North America." N Engl J Med 357(21): 2133-2142.

22. Silbermann R, Roodman GD. Myeloma bone disease: Pathophysiology and management. J Bone Oncol. 2013;2(2):59–69. Published 2013 Apr 18. doi:10.1016/j.jbo.2013.04.001.

23. Papadopoulou EC, Batzios SP, Dimitriadou M, Perifanis V, Garipidou V. Multiple myeloma and bone disease: pathogenesis and current therapeutic approaches. Hippokratia. 2010;14(2):76–81.

24. Terpos, E., et al. (2013). "International Myeloma Working Group recommendations for the treatment of multiple myeloma-related bone disease." J Clin Oncol 31(18): 2347-2357.

25. Angela Oranger, Claudia Carbone, Maddalena Izzo, and Maria Grano, “Cellular Mechanisms of Multiple Myeloma Bone Disease,” Clinical and Developmental Immunology, vol. 2013, Article ID 289458, 11 pages, 2013. https://doi.org/10.1155/2013/289458.

26. Eda, H., et al. (2016). "Bone Disease in Multiple Myeloma." Cancer Treat Res 169: 251-270.

27. van Andel, H., et al. (2017). "Aberrantly expressed LGR4 empowers Wnt signaling in multiple myeloma by hijacking osteoblast-derived R-spondins." Proc Natl Acad Sci U S A 114(2): 376-381.

28. Brunetti, G., et al. (2011). "Sclerostin is overexpressed by plasma cells from multiple myeloma patients." Ann N Y Acad Sci 1237: 19-23.

29. Visconti, R. (2020). Molecular Signaling of Multiple Myeloma. Previously unpublished.

30. Steiner, N., et al. (2015). "Marine compounds inhibit growth of multiple myeloma in vitro and in vivo." Oncotarget 6(10): 8200-8209.

31. Below J, M Das J. Vincristine. [Updated 2019 Oct 21]. In: StatPearls [Internet]. Treasure Island (FL): StatPearls Publishing; 2019 Jan-. Available from: https://www.ncbi.nlm.nih.gov/books/NBK537122/

32. Johnson-Arbor K, Patel H, Dubey R. Doxorubicin. [Updated 2019 Nov 4]. In: StatPearls [Internet]. Treasure Island (FL): StatPearls Publishing; 2019 Jan-. Available from: https://www.ncbi.nlm.nih.gov/books/NBK459232/

33. Ramamoorthy, S. and J. A. Cidlowski (2016). "Corticosteroids: Mechanisms of Action in Health and Disease." Rheum Dis Clin North Am 42(1): 15-31, vii.

34. Nooka, A. K., et al. (2019). "Daratumumab in multiple myeloma." Cancer 125(14): 2364-2382.

35. Gandolfi, S., et al. (2017). "The proteasome and proteasome inhibitors in multiple myeloma." Cancer Metastasis Rev 36(4): 561-584.

36. Harada, T., et al. (2016). "Histone deacetylase inhibitors in multiple myeloma: from bench to bedside." Int J Hematol 104(3): 300-309.

37. Laubach, J. P., et al. (2017). "Daratumumab, Elotuzumab, and the Development of Therapeutic Monoclonal Antibodies in Multiple Myeloma." Clin Pharmacol Ther 101(1): 81-88.

38. Rajkumar SV. Multiple myeloma: 2016 update on diagnosis, risk-stratification, and management. Am J Hematol. 2016 Jul;91(7):719-34. doi: 10.1002/ajh.24402. PMID: 27291302; PMCID: PMC5291298.

39. Wu, X., et al. (2003). "Osteoclast apoptosis: the role of Fas in vivo and in vitro." Endocrinology 144(12): 5545-5555.

40. Riggs, M. M. and S. Cremers (2019). "Pharmacometrics and systems pharmacology for metabolic bone diseases." Br J Clin Pharmacol 85(6): 1136-1146.

41. Chantry, A. D., et al. (2010). "Inhibiting activin-A signaling stimulates bone formation and prevents cancer-induced bone destruction in vivo." J Bone Miner Res 25(12): 2633-2646.

42. Kawai, M., et al. (2011). "Emerging therapeutic opportunities for skeletal restoration." Nat Rev Drug Discov 10(2): 141-156.

43. Hanley, D. A., et al. (2012). "Denosumab: mechanism of action and clinical outcomes." Int J Clin Pract 66(12): 1139-1146.

44. Ueno, M., Maeno, T., Nishimura, S. et al. Alendronate inhalation ameliorates elastase-induced pulmonary emphysema in mice by induction of apoptosis of alveolar macrophages. Nat Commun 6, 6332 (2015). https://doi.org/10.1038/ncomms7332

45. Jakubikova, J., et al. (2016). "A novel 3D mesenchymal stem cell model of the multiple myeloma bone marrow niche: biologic and clinical applications." Oncotarget 7(47): 77326-77341.

46. Belloni, D., et al. (2018). "Modeling multiple myeloma-bone marrow interactions and response to drugs in a 3D surrogate microenvironment." Haematologica 103(4): 707-716.

47. Hanna, H., et al. (2018). "In vitro osteoblastic differentiation of mesenchymal stem cells generates cell layers with distinct properties." Stem Cell Res Ther 9(1): 203.

48. Castillo Diaz, L. A., et al. (2016). "Osteogenic differentiation of human mesenchymal stem cells promotes mineralization within a biodegradable peptide hydrogel." J Tissue Eng 7: 2041731416649789.

49. Yu, L., et al. (2018). "3D Culture of Bone Marrow-Derived Mesenchymal Stem Cells (BMSCs) Could Improve Bone Regeneration in 3D-Printed Porous Ti6Al4V Scaffolds." Stem Cells Int 2018: 2074021.

50. Penolazzi, L., et al. (2016). "Establishment of a 3D-dynamic osteoblasts-osteoclasts co-culture model to simulate the jawbone microenvironment in vitro." Life Sci 152: 82-93.

51. Manolagas, S. C. (2000). "Birth and death of bone cells: basic regulatory mechanisms and implications for the pathogenesis and treatment of osteoporosis." Endocr Rev 21(2): 115-137.

52. Heerva, E., et al. (2014). "Follow-up of six patients with neurofibromatosis 1-related osteoporosis treated with alendronate for 23 months." Calcif Tissue Int 94(6): 608-612.

53. Ferreira, A., et al. (2015). "Bone remodeling markers and bone metastases: From cancer research to clinical implications." Bonekey Rep 4: 668.

54. Wattanachanya, L., et al. (2015). "Assessing the osteoblast transcriptome in a model of enhanced bone formation due to constitutive Gs-G protein signaling in osteoblasts." Exp Cell Res 333(2): 289-302.

55. Bar-Shavit, Z. (2007). "The osteoclast: a multinucleated, hematopoietic-origin, bone-resorbing osteoimmune cell." J Cell Biochem 102(5): 1130-1139.

56. Petrusca, D. N., et al. (2018). "Growth factor independence 1 expression in myeloma cells enhances their growth, survival, and osteoclastogenesis." J Hematol Oncol 11(1): 123.

57. Smejkal GB, Kaul CA. Stability of Nitroblue Tetrazolium-based Alkaline Phosphatase Substrates. Journal of Histochemistry & Cytochemistry. 2001;49(9):1189-1190. doi:10.1177/002215540104900914.

58. Tyrer, P., et al. (2003). "Validation and quantitation of an in vitro M-cell model." Biochemical and biophysical research communications 299: 377-383.

59. Virtanen, P. and K. Isotupa (1980). "Staining properties of alizarin red S for growing bone in vitro." Cells Tissues Organs 108(2): 202-207.

60. Rosset EM, Bradshaw AD. SPARC/osteonectin in mineralized tissue. Matrix Biol. 2016;52-54:78-87. doi:10.1016/j.matbio.2016.02.001.

61. Paschalis EP, Mendelsohn R, Boskey AL. Infrared assessment of bone quality: a review. Clin Orthop Relat Res. 2011;469(8):2170-2178. doi:10.1007/s11999-010-1751-4.

62. Boskey A, Pleshko Camacho N. FT-IR imaging of native and tissue-engineered bone and cartilage. Biomaterials. 2007;28(15):2465-2478. doi:10.1016/j.biomaterials.2006.11.043.

63. Perilli E, Parkinson IH, Reynolds KJ. Micro-CT examination of human bone: from biopsies towards the entire organ. Ann Ist Super Sanita. 2012;48(1):75-82. doi:10.4415/ANN_12_01_13.

64. Silbermann R, Roodman GD. Myeloma bone disease: Pathophysiology and management. J Bone Oncol. 2013;2(2):59–69. Published 2013 Apr 18. doi:10.1016/j.jbo.2013.04.001.

65. Silvestris F, Cafforio P, De Matteo M, Calvani N, Frassanito MA, Dammacco F. Negative regulation of the osteoblast function in multiple myeloma through the repressor gene E4BP4 activated by malignant plasma cells. Clin Cancer Res. 2008 Oct 1;14(19):6081-91. doi: 10.1158/1078-0432.CCR-08-0219. PMID: 18829486.

66. Seckinger A, Meissner T, Moreaux J, et al. Bone morphogenic protein 6: a member of a novel class of prognostic factors expressed by normal and malignant plasma cells inhibiting proliferation and angiogenesis. Oncogene. 2009;28(44):3866-3879. doi:10.1038/onc.2009.257.

67. Grcević D, Kusec R, Kovacić N, Lukić A, Lukić IK, Ivcević S, Nemet D, Seiwerth RS, Ostojić SK, Croucher PI, Marusić A. Bone morphogenetic proteins and receptors are over-expressed in bone-marrow cells of multiple myeloma patients and support myeloma cells by inducing ID genes. Leuk Res. 2010 Jun;34(6):742-51. doi: 10.1016/j.leukres.2009.10.016. Epub 2009 Nov 18. PMID: 19926132.

68. Gooding, S., Olechnowicz, S.W.Z., Morris, E.V. et al. Transcriptomic profiling of the myeloma bone-lining niche reveals BMP signalling inhibition to improve bone disease. Nat Commun 10, 4533 (2019). https://doi.org/10.1038/s41467-019-12296-1.

69. Jaquiéry C, Schaeren S, Farhadi J, et al. In vitro osteogenic differentiation and in vivo bone-forming capacity of human isogenic jaw periosteal cells and bone marrow stromal cells. Ann Surg. 2005;242(6):859-868. doi:10.1097/01.sla.0000189572.02554.2c.

70. Yu, L., et al. (2018). "3D Culture of Bone Marrow-Derived Mesenchymal Stem Cells (BMSCs) Could Improve Bone Regeneration in 3D-Printed Porous Ti6Al4V Scaffolds." Stem Cells International 2018: 2074021.

71. Owen R, Reilly GC. In vitro Models of Bone Remodelling and Associated Disorders. Front Bioeng Biotechnol. 2018;6:134. Published 2018 Oct 11. doi:10.3389/fbioe.2018.00134.

72. Kohli N, Ho S, Brown SJ, Sawadkar P, Sharma V, Snow M, García-Gareta E. Bone remodelling in vitro: Where are we headed?: -A review on the current understanding of physiological bone remodelling and inflammation and the strategies for testing biomaterials in vitro. Bone. 2018 May;110:38-46. doi: 10.1016/j.bone.2018.01.015. Epub 2018 Feb 3. PMID: 29355746.

73. Lopa S., Bongio M., Gilardi M., Bersini S., Mondadori C., and Moretti M. Development of a Miniaturised 3D Bone Remodelling Model Embedding Precursors of Human Osteoblast and Osteoclast in a Vascularised CAP Nanoparticle-Enriched Hydrogel Matrix. Orthopaedic Proceedings 2017 99-B:SUPP_1, 35-35.

74. Ham J, Lever L, Fox M, Reagan MR. In Vitro 3D Cultures to Reproduce the Bone Marrow Niche. JBMR Plus. 2019;3(10):e10228. Published 2019 Oct 1. doi:10.1002/jbm4.10228.

75. Belloni D, Heltai S, Ponzoni M, et al. Modeling multiple myeloma-bone marrow interactions and response to drugs in a 3D surrogate microenvironment. Haematologica. 2018;103(4):707-716. doi:10.3324/haematol.2017.167486.

76. Garrett, I. R., et al. (1997). "A murine model of human myeloma bone disease." Bone 20(6): 515-520.

77. Syed Mehdi, Maurizio Zangari, Donghoon Yong; An Improved Animal Model of Multiple Myeloma Bone Disease. Blood 2020; 136 (Supplement 1): 31. doi: https://doi.org/10.1182/blood-2020-142928

78. I. Moreno-Jimenez, A. Cipitria, A. Sanchez-Herrero, A. F. Van Tol, A. Roschger, C. A. Lahr, J. A. McGovern, D. W. Hutmacher, P. Fratzl. Human and mouse bones physiologically integrate in a humanized mouse model while maintaining species-specific ultrastructure. Science Advances. 28 OCT 2020 : EABB9265

79. Michelle M. McDonald, Michaela R. Reagan, Scott E. Youlten, Sindhu T. Mohanty, Anja Seckinger, Rachael L. Terry, Jessica A. Pettitt, Marija K. Simic, Tegan L. Cheng, Alyson Morse, Lawrence M. T. Le, David Abi-Hanna, Ina Kramer, Carolyne Falank, Heather Fairfield, Irene M. Ghobrial, Paul A. Baldock, David G. Little, Michaela Kneissel, Karin Vanderkerken, J. H. Duncan Bassett, Graham R. Williams, Babatunde O. Oyajobi, Dirk Hose, Tri G. Phan, Peter I. Croucher; Inhibiting the osteocyte-specific protein sclerostin increases bone mass and fracture resistance in multiple myeloma. Blood 2017; 129 (26): 3452–3464. doi: https://doi.org/10.1182/blood-2017-03-773341.

80. Heath DJ, Chantry AD, Buckle CH, Coulton L, Shaughnessy JD Jr, Evans HR, Snowden JA, Stover DR, Vanderkerken K, Croucher PI. Inhibiting Dickkopf-1 (Dkk1) removes suppression of bone formation and prevents the development of osteolytic bone disease in multiple myeloma. J Bone Miner Res. 2009 Mar;24(3):425-36. doi: 10.1359/jbmr.081104. PMID: 19016584.

81. Bjorklund, C. C., et al. (2011). "Evidence of a role for activation of Wnt/beta-catenin signaling in the resistance of plasma cells to lenalidomide." The Journal of biological chemistry 286(13): 11009-11020.

82. Raje N, Terpos E, Willenbacher W, Shimizu K, García-Sanz R, Durie B, Legieć W, Krejčí M, Laribi K, Zhu L, Cheng P, Warner D, Roodman GD. Denosumab versus zoledronic acid in bone disease treatment of newly diagnosed multiple myeloma: an international, double-blind, double-dummy, randomised, controlled, phase 3 study. Lancet Oncol. 2018 Mar;19(3):370-381. doi: 10.1016/S1470-2045(18)30072-X. Epub 2018 Feb 9. PMID: 29429912.

83. Nishida H. Bone-targeted agents in multiple myeloma. Hematol Rep. 2018;10(1):7401. Published 2018 Mar 29. doi:10.4081/hr.2018.7401.

Appendix

Supplemental Materials

3D Normal Bone Model Cells

Mesenchymal Stem Cells (Rooster Bio, cat# MSC-030)

Human Osteoclast Precursors (Lonza, cat# 2T-110)

Bone Marrow Stromal Cell/Mesenchymal Stem Cell Medium

hMSC High Performance Media Kit XF (Rooster Bio, cat# KT-016)

Osteoblast Differentiation Medium

OsteoMax XF (EMD Millipore, cat# SCM121)

Osteoclast Differentiation Medium

Mesenchymal Stem Cell Growth Medium (MSCGM) (Lonza, cat# PT-3001)

RANKL 66.66 ng/ml (Sigma-Aldrich, cat# GF091)

M-CSF 33.33 ng/ml (Sigma-Aldrich, cat# SRP6165-10UG)

3D Human Bone Model Medium

1:1 Mix of OsteoMax XF and Osteoclast medias

Supplemental Reagents

Growth Factor-Reduced Matrigel (Corning, cat# 354230)

Human Multiple Myeloma-Derived Cell Lines:

- NCI-H929 (ATCC CRL-9068) human plasmacytoma
- RPMI-8226 (ATCC CRM-CCL-155) human plasmacytoma
- MM.1S (ATCC CRL-2974) human myeloma
- U266 (ATCC TIB-196) human plasmacytoma

MM Medium

RPMI-1640 (Gibco, cat# 11875), Fetal Bovine Serum (Gibco, cat# 10082)

MBD Complete Medium

OsteoMaxXF: Osteoclast Differentiation Medium: MM Medium (RPMI-1640+ 10%FBS)

Alkaline Phosphatase Staining Reagents

NBT/BCIP Ready-to-Use Tablets Protocol & Troubleshooting

Product No. **11697471001**

Protocol

Recommended counterstains for non-radioactive in situ hybridization in combination with Anti-DIG-AP detection/NBT/BCIP:

It is a well-known phenomenon that NBT/BCIP is not compatible with classical counterstains. NBT/BCIP signals should not be mounted with xylene-containing mounting media, such as DPX, because these could lead to crystal formations of the color precipitates. Unfortunately, classical counterstains, such as eosin require xylene-containing mounting media.

The following mounting reagents are specifically available for mounting sections with NBT/BCIP signals: Crystalmount from Biomedia or Vectamount or Immunomount from Vector Laboratories. The same companies also offer organic counterstains which are compatible with these mounting media (e.g.,Vector Methyl Green, Vector Nuclear Fast Red).

The results of combining a particular counterstain with any of the mounting media primarily depends on the type of tissue used for NBT/BCIP color detection.

Staining adjacent slides with or, without NBT/BCIP detection with a typical counterstain and to mount the slides with the classical xylene-containing mounting medium. This allows the direct comparison of stained tissue with or, without signal.

Customer Recommended Protocol* for the Preparation of a mounting medium:

Glycerol gelatin:

- 100 ml of 0.2 M phosphate buffer pH 7;
- Na azide 200 mg;
- gelatin 15 g, stir until dissolved;
- glycerol 100 ml.

Keep at +37 °C, add a drop to the slide and coverslip. After hardening of the mounting media, the signal is said to last for several years without fading of the NBT/BCIP precipitate.

OsteoImage Assay Protocol Details

. The OsteoImage™ Assay requires a fluorescence microscope or plate reader capable of excitation/emission at approximately 492nm and 520nm, respectively.

. Black-walled plates are recommended for assays using OsteoImage™; however, clear plates can be used.

. OsteoImage™ performs equally well on cells fixed with either cross-linking or denaturing fixatives (e.g. formaldehyde or alcohols).

Cell Culture Notes

. Different osteoblast cell types require varying methods and lengths of time for differentiation and for mineralization.

. If using a related Lonza cell product, refer to the Instructions for Use specific for that cell type for culture suggestions.

Preparation of reagents:

1. Calculate the total volume of OsteoImage™ Wash Buffer required for 5 wash steps (see Table 1 for suggested volumes per well). Dilute the 10x stock Wash Buffer 1:10 in deionized water at the final volume calculated (alternatively, the entire stock can be diluted for a 500 ml total volume and stored at room temperature or 4oC for future use).
2. Calculate the total volume of OsteoImage™ Staining Reagent needed based on number of wells and well size (see Table 1). Dilute Staining Reagent 1:100 in Staining Reagent Dilution Buffer to the final calculated volume. Mix well and keep protected from light

Protocol for Staining & Assay:

1. When cells are ready to be evaluated for mineralization, remove culture plate from incubator and allow cooling to room temperature.
2. Remove media and wash once with PBS.
3. Fix cells using appropriate fixative method (e.g. Incubation with ethanol for 20 minutes).
4. After fixation, rinse 1-2 times with diluted (1X) Wash Buffer.
5. Add appropriate amount (See Table 1) of diluted Staining Reagent to each well.
6. Incubate at room temperature, protected from the light, for 30 minutes.
7. After incubation step, remove the Staining Reagent from wells and discard. Wash 3 times with the appropriate volume (see Table 1) of diluted Wash Buffer, leaving wash buffer in the wells for ~5 minutes per wash.
8. After final wash, add Wash Buffer to each well for microscope viewing or plate reader analysis according to volumes in Table 1.
9. View under appropriate excitation and emission settings on fluorescence microscope (e.g. Fluorescein filter set).
10. If performing quantitative assay using fluorescent plate reader, choose appropriate excitation/emission wavelengths (492/520) and plate layout before reading plate.

Table 1 Wells/ Plate	Volume of Diluted Staining Reagent/well	Volume of Diluted Wash Buffer/well
6-well	1.0ml	2.0ml
12-well	0.75ml	1.5ml

24-well	0.5ml	1.0ml
48-well	0.2ml	0.4ml
96-well	0.1ml	0.2ml

Type I Collagen C-telopeptide, CTX-I, Assay Kit (Chondrex Inc, Catalog # 6033)

CTX-I Assay Outline